ASTROBIOLOGY
Volume 17, Number 11, 2017

DOI: 10.1089/ast.2016.1606

The Lost City Hydrothermal Field: A Spectroscopic and Astrobiological Analogue for Nili Fossae, Mars

Elena S. Amador,[1] Joshua L. Bandfield,[2] William J. Brazelton,[3] and Deborah Kelley[4]

Abstract

Low-temperature serpentinization is a critical process with respect to Earth's habitability and the Solar System. Exothermic serpentinization reactions commonly produce hydrogen as a direct by-product and typically produce short-chained organic compounds indirectly. Here, we present the spectral and mineralogical variability in rocks from the serpentine-driven Lost City Hydrothermal Field on Earth and the olivine-rich region of Nili Fossae on Mars. Near- and thermal-infrared spectral measurements were made from a suite of Lost City rocks at wavelengths similar to those for instruments collecting measurements of the martian surface. Results from Lost City show a spectrally distinguishable suite of Mg-rich serpentine, Ca carbonates, talc, and amphibole minerals. Aggregated detections of low-grade metamorphic minerals in rocks from Nili Fossae were mapped and yielded a previously undetected serpentine exposure in the region. Direct comparison of the two spectral suites indicates similar mineralogy at both Lost City and in the Noachian (4–3.7 Ga) bedrock of Nili Fossae, Mars. Based on mapping of these spectral phases, the implied mineralogical suite appears to be extensive across the region. These results suggest that serpentinization was once an active process, indicating that water and energy sources were available, as well as a means for prebiotic chemistry during a time period when life was first emerging on Earth. Although the mineralogical assemblages identified on Mars are unlikely to be directly analogous to rocks that underlie the Lost City Hydrothermal Field, related geochemical processes (and associated sources of biologically accessible energy) were once present in the subsurface, making Nili Fossae a compelling candidate for a once-habitable environment on Mars. Key Words: Mars—Habitability—Serpentinization—Analogue. Astrobiology 17, 1138–1160.

1. Introduction

The search for habitable environments in our solar system is commonly driven by evidence for environments with liquid water. However, water alone is not sufficient to sustain life. Temperature and pH gradients, nutrients, and a source of biologically accessible energy are also critical. Environments with active serpentinization, which involves the interaction of water with ultramafic rock, can host ecosystems driven predominantly by chemical energy harnessed from these alteration processes (*e.g.,* Kelley *et al.,* 2001, 2005; Früh-Green *et al.,* 2004; Russell *et al.,* 2010). Serpentinization has been documented in several Earth settings, including the deep-sea hydrothermal vent system of the Lost City Hydrothermal Field (Kelley *et al.,* 2001, 2005; Früh-Green *et al.,* 2004) and the high-temperature Rainbow and Logatchev Hydrothermal Fields (Holm and Charlou, 2001; Petersen *et al.,* 2009) on the Mid-Atlantic Ridge, as well as at numerous ophiolite complexes (*e.g.,* Barnes *et al.,* 1978; O'Hanley, 1996; Früh-Green *et al.,* 2004). Spectroscopic studies of Mars have also shown evidence for serpentine-bearing surfaces, implying that serpentinization was an active process at some point in the planet's history (*e.g.,* Ehlmann *et al.,* 2009, 2010).

This study characterizes the spectral and mineralogical variability in mafic bedrock samples and their alteration products from beneath the Lost City Hydrothermal Field on the Mid-Atlantic Ridge and compares these results with mineralogically similar exposures at Nili Fossae, Mars. Results are placed into a geochemical and astrobiological context for processes that operated on Mars with implications for existing and future measurements acquired by orbital and landed spacecraft on Mars. Results from this study may also inform future science and instrumentation for astrobiologically relevant missions to Mars.

[1]Department of Earth and Space Sciences, University of Washington, Seattle, Washington.
[2]Space Science Institute, Boulder, Colorado.
[3]Department of Biology, University of Utah, Salt Lake City, Utah.
[4]School of Oceanography, University of Washington, Seattle, Washington.

1.1. Serpentinization

Serpentinization is an exothermic, volume-increasing reaction caused by the reduction of H_2O by ferrous iron in ultramafic rocks (Reactions 1–3) (O'Hanley, 1996; Evans, 2010). The reaction enriches altered fluids in H_2 and CH_4 and other low-molecular-weight hydrocarbons that can be metabolically exploited by microorganisms (Abrajano *et al.,* 1988; Kelley *et al.,* 2001, 2005; Proskurowski *et al.,* 2006, 2008; Brazelton *et al.,* 2010; Lang *et al.,* 2010; Etiope *et al.,* 2011; Klein and McCollom, 2013). The reactions occur over a wide range of conditions that include penetration by meteoric and marine fluids, and at 200°C to >500°C temperatures (Evans, 1977; Früh-Green *et al.,* 2004).

The serpentinization process is ideally composed of three reactions:

Reaction 1

$$\text{Fayalite} + \text{water} \rightarrow \text{magnetite} + \text{aqueous silica} + \text{hydrogen}$$

$$3Fe_2SiO_4 + 2H_2O \rightarrow 2Fe_3O_4 + 3SiO_2 + 2H_2$$

Reaction 2

$$\text{Forsterite} + \text{silica} + \text{water} \rightarrow \text{serpentine}$$

$$3Mg_2SiO_4 + SiO_2 + 4H_2O \rightarrow 2Mg_3Si_2O_5(OH)_4$$

Reaction 3

$$\text{Forsterite} + \text{water} \rightarrow \text{serpentine} + \text{brucite}$$

$$2Mg_2SiO_4 + 3H_2O \rightarrow Mg_3Si_2O_5(OH)_4 + Mg(OH)_2$$

Subsequent production of methane is also common in serpentinizing systems but requires introduction of a carbon source (*e.g.,* Kelley and Früh-Green, 1999; Charlou *et al.,* 2002; Früh-Green *et al.,* 2004; Proskurowski *et al.,* 2008), for example:

Reaction 4

$$4H_2 + CO_2 \rightarrow CH_4 + 2H_2O$$

Ultramafic rocks are dominated by olivine with lesser orthopyroxene minerals; these phases are thermodynamically stable at high temperatures and pressures, as in the mantle. However, when these rocks are brought to the near surface, as at some tectonic margins or as komatiites, for example, they are unstable and consequently readily react with aqueous fluids (*e.g.,* Evans, 1977; Früh-Green *et al.,* 2004; Schulte *et al.,* 2006). Because the reactions are exothermic and result in an increase in the rock volume by up to 55% (O'Hanley, 1996), serpentinization may result in enhanced fracturing that promotes fluid flow and alteration (*e.g.,* Kelley *et al.,* 2001, 2005; Lowell and Rona, 2002; Vance *et al.,* 2007; Denny *et al.,* 2016).

Serpentinization produces hydrous Fe/Mg-serpentine phases that may be represented by the general formula $(Mg, Fe^{2+})_3(Si_2O_5)(OH)_4$. The three most common polymorphs are the Mg-rich phases antigorite, chrysotile, and lizardite. Other mineralogical products include magnetite and brucite. The reactions produce highly alkaline fluids due to an increase in OH^- from the dissolution of olivine and pyroxene; these fluids commonly lead to the precipitation of carbonate from both meteoric and marine solutions (O'Hanley, 1996; Früh-Green *et al.,* 2003; Palandri and Reed, 2004; Ludwig *et al.,* 2006).

Most relevant to astrobiology, the oxidation of Fe^{2+} (mostly from fayalite, the Fe-olivine end-member) is responsible for the production of highly reducing molecular hydrogen (H_2) (*e.g.,* Neal and Stanger, 1983; Neubeck *et al.,* 2014), which is then biologically accessible for microbial metabolic pathways, such as methanogenesis (Früh-Green *et al.,* 2004). Zones of active serpentinization, therefore, create habitable environments where other energy sources may not be available (*e.g.,* solar or volcanic) and promote ecosystems driven by the direct products of these geochemical reactions. Serpentinization is likely to have occurred throughout much of Earth's history and may have potentially created environments suitable for the origin of life on early Earth (Kelley *et al.,* 2005; Martin *et al.,* 2008; Russell *et al.,* 2010, 2014; Stüeken *et al.,* 2013; Sojo *et al.,* 2016). Given the common association of liquid water in direct contact with olivine-rich bedrock on Earth, similar geochemical environments are likely present across the Solar System, including the icy satellites of Jupiter and Saturn. These moons likely have olivine-rich mantles in contact with liquid-water oceans and are compelling sites to visit for potential extant life in our solar system (*e.g.,* Malamud and Prialnik, 2013; Russell *et al.,* 2014).

Products of serpentinization can be detected with infrared spectrometers (*e.g.,* Brown *et al.,* 2005; Bishop *et al.,* 2008; Ehlmann *et al.,* 2010), including instrumentation on airplanes and orbital spacecraft. Planetary surfaces with serpentine-bearing phases have unique spectral absorptions in near-infrared (NIR) reflectance and thermal-infrared (TIR) emissivity (defined here as ~1.0–3.0 μm and 5.0–50.0 μm, respectively) spectra, allowing for the confident identification of serpentine (*e.g.,* Ehlmann *et al.,* 2010). Furthermore, given that serpentine is created via reactions that typically produce H_2 in the presence of liquid water, the identification of serpentine phases is a unique indicator for two of the three components commonly assumed necessary for a habitable environment: an energy source (H_2), a solvent (liquid water), and nutrients (*e.g.,* Domagal-Goldman and Wright *et al.,* 2016). Other phases associated with serpentinization, such as talc, also have spectral characteristics in the NIR and TIR portions of the spectrum. In concert, analyses that span the NIR and TIR provide a more complete understanding of the full range of compositions present in a rock or planetary surface and clues about the paleoenvironment present during their formation and alteration history.

1.2. The Lost City Hydrothermal Field, Earth

1.2.1. Geology. The Lost City Hydrothermal Field is a submarine hydrothermal venting system located near the summit of the Atlantis Massif, ~15 km west of the slow-spreading Mid-Atlantic Ridge near 30°N (Kelley *et al.,* 2001, 2005). The Atlantis Massif is part of a larger ultramafic oceanic core complex composed of uplifted, serpentinized mantle peridotites (*e.g.,* Denny *et al.,* 2016). The terrain is highly fractured with a complex tectonic history

not uncommon for sites located near slow- and ultra-slow-spreading centers (Kelley *et al.,* 2005; Karson *et al.,* 2006; Denny *et al.,* 2016). The Lost City was serendipitously discovered in 2000 (Kelley *et al.,* 2001) and includes numerous actively venting limestone monoliths that rise 30–60 m above the surrounding seafloor. It has been active for at least 150,000 years (Ludwig *et al.,* 2011) and hosts a robust microbial community driven by hydrothermal fluids whose chemistry is determined by serpentinization reactions in the subsurface (Schrenk *et al.,* 2004; Kelley *et al.,* 2005; Brazelton *et al.,* 2006, 2010; Proskurowski *et al.,* 2008). It is one of only a few detected carbonate-dominated hydrothermal systems, where the alteration of the olivine-rich protolith provides biologically viable energy for microbial life (*e.g.,* Schrenk *et al.,* 2004; Brazelton *et al.,* 2006, 2010).

Faulting of the Atlantis Massif exposes massive serpentinite with lesser gabbro in the bedrock that underlies the Lost City Hydrothermal Field and in adjacent cliffs. In this area, >70% of the exposed rocks are variably altered and deformed serpentinized harzburgites, an ultramafic igneous rock composed primarily of olivine and low-Ca pyroxene (Boschi *et al.,* 2006; Karson *et al.,* 2006; Denny *et al.,* 2016). Serpentine mineral assemblages are predominantly lizardite, with or without chrysotile and trace amounts of antigorite (Boschi *et al.,* 2006). Talc, chlorite, and tremolite are also found in association with the serpentine phase (Boschi *et al.,* 2006). The summit of the massif is capped by pelagic carbonate (Kelley *et al.,* 2001; Früh-Green *et al.,* 2003; Denny *et al.,* 2016). The field is enclosed by a halo of carbonate rubble from chimneys associated with the active and extinct vents (Kelley *et al.,* 2005; Ludwig *et al.,* 2006; Denny *et al.,* 2016).

The Lost City Hydrothermal Field serpentinites, and associated alteration products, are produced by the hydration and oxidation of the underlying ultramafic rocks (Kelley *et al.,* 2001, 2005; Boschi *et al.,* 2006; Delacour *et al.,* 2008). Isotopic analyses indicate that the fluid/rock interactions typically occur at temperatures <150°C (Früh-Green *et al.,* 2003; Proskurowski *et al.,* 2006) and produce pH 9–11 vent fluids enriched in H_2, CH_4, and other low-molecular-weight hydrocarbons (*e.g.,* ethane (C_2H_6), ethylene (C_2H_4), and propane (C_3H_8)) (Kelley *et al.,* 2001, 2005; Proskurowski *et al.,* 2006, 2008; Lang *et al.,* 2010). When the alkaline fluids mix with seawater, carbonate ions combine with Ca^{2+} ions, resulting in the precipitation of aragonite (Früh-Green *et al.,* 2003; Ludwig *et al.,* 2006). The Mg-rich mineral brucite also precipitates. During aging of the structures, brucite is lost, and the metastable aragonite converts to calcite (Ludwig *et al.,* 2006, 2011). Dating of the limestone deposits indicates that the field has been active for >120,000 years (Ludwig *et al.,* 2011).

1.2.2. Biodiversity. A thriving microbial ecosystem was discovered at the Lost City Hydrothermal Field, presumably sustained by the geochemical products of serpentinization, hydrothermal flow, and mixing with seawater (Kelley *et al.,* 2001, 2005; Schrenk *et al.,* 2004; Brazelton *et al.,* 2006, 2010). Extensive biofilms are developed on mineral surfaces within the carbonate structures (*e.g.,* Kelley *et al.,* 2001; Schrenk *et al.,* 2004; Brazelton *et al.,* 2011). Microbial communities representing all three domains of life (Brazelton *et al.,* 2006, 2010; López-Garcia *et al.,* 2007) are found throughout the chimneys, from the mesophilic (~25°C), aerobic surfaces to the (hyper)thermophilic (50–90°C), anaerobic zones of the chimney interiors (Kelley *et al.,* 2001; Schrenk *et al.,* 2004). The resident microbial communities are stimulated by the abundant chemical energy available from serpentinization (Brazelton *et al.,* 2011). This energy is approximately twice that available at basalt-hosted black smokers due to the higher concentration of H_2 (McCollom and Seewald, 2007) in serpentinization-driven systems.

1.3. Nili Fossae, Mars

The Nili Fossae are a set of concentric graben-forming fractures to the west of the Isidis Basin and to the north of the Syrtis Major volcanic complex (Fig. 1). The fractures and faulting likely formed due to flexure and unloading associated with the Isidis Basin–forming impact (Wichman and Schultz, 1989; Schultz and Frey, 1990), which occurred ~3.9 billion years ago (Frey, 2003). This mid-Noachian impact event occurred during a period when hydrous alteration of crustal rocks was occurring globally on Mars (*e.g.,* Carr and Head, 2010). Extensive exposures of olivine-rich bedrock occur within, and in proximity to, Nili Fossae (*e.g.,* Hoefen *et al.,* 2003), which is observable from orbit (Ruff and Christensen, 2002).

A diverse range of both primary and alteration minerals have been documented in the region (*e.g.,* Poulet *et al.,* 2005; Bibring *et al.,* 2006; Mangold *et al.,* 2007; Mustard *et al.,* 2007, 2009; Ehlmann *et al.,* 2008, 2009, 2010; Tornabene *et al.,* 2008), including an assemblage of phases associated with low-grade metamorphism (*e.g.,* Ehlmann *et al.,* 2009, 2010; Brown *et al.,* 2010; Viviano *et al.,* 2013). These include serpentine, which has been identified by spectroscopic measurements in several locations across Mars (Ehlmann *et al.,* 2010; Viviano-Beck and Murchie, 2014). However, the presence of serpentine phases in Nili Fossae is unique because they are found within a well-defined stratigraphic context. The eastern Nili Fossae bedrock is composed of three major bulk compositions. Moving from bottom to top of the section, the lowermost unit is composed of an olivine-poor basalt with an Fe/Mg-phyllosilicate component consistent with nontronite, followed by an olivine-rich basalt that has been variably altered to Mg carbonate, serpentine, and talc and/or saponite, and an olivine-poor basaltic capping unit with localized hydration and alteration resulting in an elevated bulk-silica composition (Amador and Bandfield, 2016) (Fig. 1).

2. Approach

Fifteen variably altered and deformed serpentinites, gabbros, fault rocks, and carbonate samples from the Lost City Hydrothermal Field were selected for spectral analysis from a set collected by the human-occupied vehicle Alvin during an oceanographic cruise in 2003 funded by the National Science Foundation (Kelley *et al.,* 2001; Table 1 and Fig. 2). The 15 samples were classified into six rock-type groups: ''serpentinite,'' ''carbonate,'' ''gabbro,'' ''talc-rich fault rock,'' ''amphibole-rich fault rock,'' and ''pelagic top-layer.'' Mineralogical and compositional analyses for the non-carbonate samples have been described by Boschi *et al.* (2006), Delacour *et al.* (2008), and Karson *et al.* (2006) and

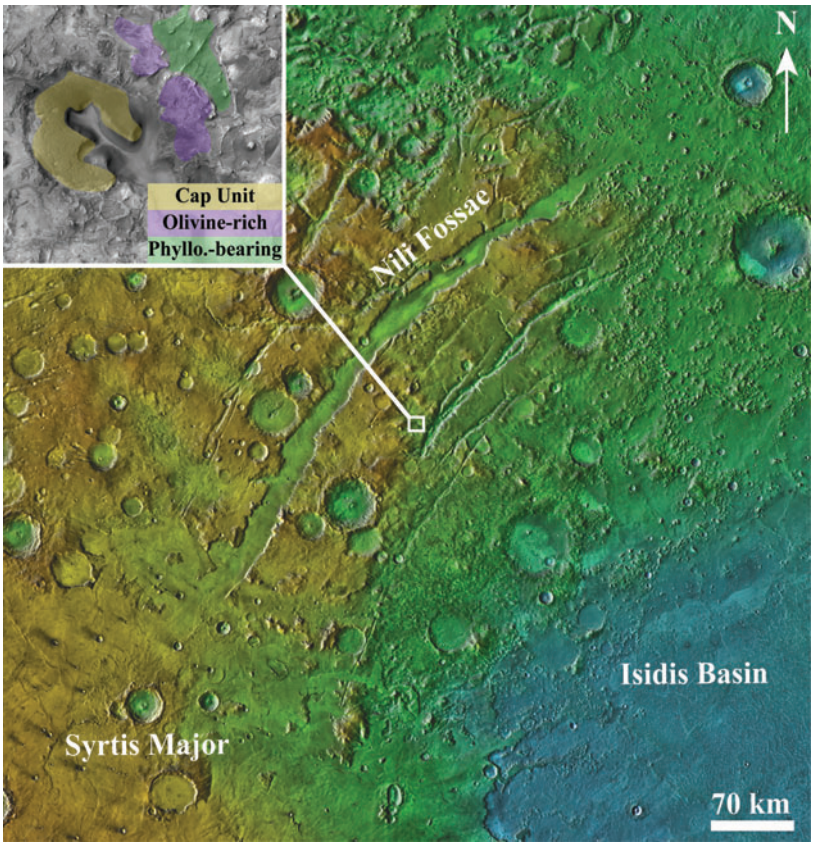

FIG. 1. Nilo-Syrtis Major colorized elevation map with THEMIS Global Day IR mosaic used for shading centered around 76.6°E, 22.4°N. Inset image shows typical Nili Fossae stratigraphy in CTX image DO1_027691_2025_XN_22N_282W.

for carbonate deposit samples by Ludwig *et al.* (2006, 2011) (Table 1) using petrographic and bulk rock geochemical methods: no NIR or TIR spectral characterizations of these rocks had been performed previously. Handheld rock descriptions for the 15 samples used for this study are provided in Table 1.

Spectral characterization of rock samples has several benefits; first, it allows for a nondestructive method of determining the mineral constituents of the rocks, unlike (for example) preparing thin sections for electron microprobe analysis, which only provides elemental abundances. Second, little sample preparation is needed, saving time and resources. Third, spectral characterization provides a library from this specific hydrothermal environment using measurements directly comparable to those acquired of other planetary surfaces. Near- and thermal-infrared spectral measurements have been collected by numerous spacecraft throughout the Solar System, including Mars (*e.g.,* CRISM/TES/THEMIS), Ceres/Vesta (Dawn VIR), Pluto (New Horizons RALPH), and Jupiter (Galileo NIMS), and they are planned for future robotic missions. These measurements are particularly useful because they can be made remotely from orbit and because they can provide a wealth of information at global, regional, and local scales. With these benefits in mind, we measured the TIR emissivity and NIR reflectance properties for Lost City samples and compared them to measurements of low-grade alteration minerals on the surface of Mars in Nili Fossae (*e.g.,* Ehlmann *et al.,* 2009; Brown *et al.,* 2010; Viviano *et al.,* 2013), which were detected with NIR reflectance measurements. These measurements also serve as a spectral library for future orbital and landed spacecraft with these measurement capabilities.

2.1. Laboratory spectral measurements

2.1.1. Thermal infrared. Thermal-infrared emissivity measurements can provide an understanding of the bulk mineralogical composition for a given rock sample. This is possible because most rock-forming minerals have major absorptions in the 200–2000 cm^{-1} (5.0–50.0 μm) range (*e.g.,* Thomson and Salisbury, 1993). Because of the implications for serpentinization and hydrothermal mineral identification, the spectral characteristics for silicate hydroxides and carbonates are of particular relevance to this work. Reststrahlen band absorptions occur between 833 and 1250 cm^{-1} (8.0 and 12.0 μm) due to vibrational motions associated with Si-O stretching modes—the exact minima for this feature depend on the mineral structure and composition (*e.g.,* Hunt and Salisbury, 1971). Additional absorptions due to Si, O, and Al stretching and bending motions occur at longer wavelengths between 250 and 833 cm^{-1} (40.0 and 12.0 μm) (Hunt, 1980). Hydroxide-bearing minerals have characteristic spectral features due to fundamental bending modes of OH-metal ions (Hunt, 1980). Carbonate minerals have strong absorption features due to CO_3 vibrational modes in the 1250–1666 cm^{-1} (6.0–8.0 μm) range (Hunt and Salisbury, 1971).

Thermal-infrared emissivity measurements allow for quantitative mineral abundances to be calculated from the whole rock spectrum. The high absorption coefficient of typical rock-forming minerals in the TIR spectral range

Table 1. Lost City Hydrothermal Field Samples with Descriptions

Sample number	*Rock type*	*Boschi* et al. *(2007) Table 1. Description*	*Delacour* et al. *(2008) Table 2. Description*	*Karson* et al. *(2006) Table 1. Description*	*Reference ID**	*Rock description (this study)*
1	Serpentinite	Serpentinite	None	Serp+amph+chl. Veins of late calcium carbonate	3872-1136	Dark-toned, heterogeneous coloring, mesh-textured, small fractures
2	Gabbro	Gabbro	None	Medium-grained gabbro	3876-1117	Dark-toned, heterogeneous, large fractures
3	Talc-rich fault rock	Talc-rich fault rock	None	Serpentinite/talc-amph schist	3873-1124	Light-toned, heterogeneous coloring, soapy feeling to touch
4	Serpentinite	None	None	Serpentinite	3873-1245	Massive, dark-toned, heterogeneous coloring, microfractures, mesh-textured
5	Gabbro	Mylonitic gabbro	None	None	3867-1254	Dark-toned, fractures filled with light-toned material
6	Serpentinite	Serpentinite	None	None	3877-1344	Heterogeneous, highly fractured with light-toned material, mesh-textured, soapy feeling to touch
7	Amphibole-rich fault rock	Amphibole-rich fault rock	None	None	3877-1313	Light-toned, heterogeneous, marbled texture
8	Serpentinite	None	Serpentinite	None	3877-1307	Heterogeneous, highly fractured with light-toned filling, mesh-textured
9	Serpentinite	Serpentinite (local metasomatism)	None	None	3877-1158	Heterogeneous, highly fractured, fractures, large alteration veins, soapy feeling to touch
10	Pelagic top-layer	None	None	None	3867-1116	Brecciated fragments in a fine-grained carbonate matrix
11	Carbonate	None	None	None	3881-1132B	Porous, fine-grained, bright white, friable
12	Carbonate	None	None	None	3867-1308	Brown colored, porous, fine-grained, fossils, friable *Described in Ludwig *et al.* (2006)
13	Carbonate	None	None	None	3869-1446	Porous, fine-grained, bright white, friable, some reddish discoloration *Described in Ludwig *et al.* (2006)
14	Pelagic top-layer	None	None	None	3862-1549 #6	Brown-colored, porous, fine-grained, friable, fossils
15	Carbonate	None	None	None	3864-1537	Bright white, friable porous, fine-grained

**Reference ID* is used across studies by others working with these samples. *Sample number* is used for this study only.

results in a spectrum that can be approximated by a linear combination of each individual mineral spectrum of the measured surface, weighted by the areal abundance of the mineral (*e.g.,* Thomson and Salisbury, 1993; Ramsey and Christensen, 1998). The TIR spectral measurements therefore serve to (a) determine the bulk mineralogy of the Lost City samples and (b) provide an understanding of the variety of TIR spectral characteristics specific to this type of hydrothermal system. The latter can be used for future data analysis and instrumentation selection on orbital and landed missions to Mars and other silicate-bearing bodies.

Thermal-infrared emissivity spectra were collected at the Thermal Emission Spectroscopy Laboratory at Arizona State University. A modified Nicolet Nexus 670 FTIR interferometric spectrometer was used to collect emission measurements between 200 and 2500 cm^{-1} (4.0 and 50.0 μm). For details regarding the instrument setup, measurement, and calibration procedures, see the work of Ruff *et al.* (1997). Rock samples were heated to ~80°C for several hours in an oven and then transferred to an N_2-purged environmental chamber where the radiance was measured via the emission port of the spectrometer. Several measurements, each with a spot size of ~1 cm^2, were made for all 15 rock samples. Different rock faces were exposed to the detector in order to capture any heterogeneity in mineralogy.

Mineral abundances were determined by using a linear deconvolution method applied to the measured TIR emissivity. This method has been shown to successfully model the

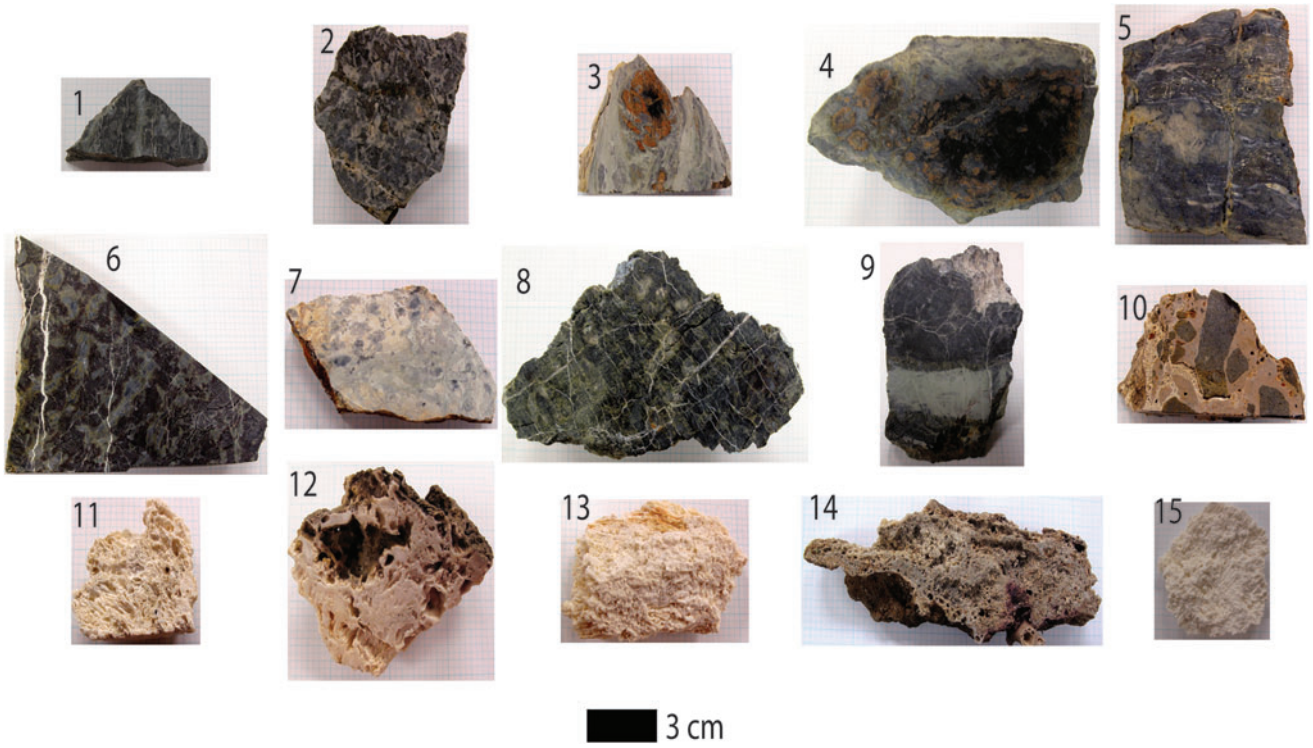

FIG. 2. Photographs of the Lost City Hydrothermal Field samples used for this study.

mineralogy for coarse particulate mixtures and rocks (Ramsey and Christensen, 1998; Feely and Christensen, 1999; Hamilton and Christensen, 2000; Rogers and Aharonson, 2008). As stated previously, this method allows for a nondestructive analysis of mineralogy with a ~5–7 vol % detection limit under optimal conditions (*e.g.,* no interfering factors due to small particle sizes and the end-member spectral library has all the correct phases present) (Ramsey and Christensen, 1998; Feely and Christensen, 1999; Hamilton and Christensen, 2000) and a fairly rapid sample-preparation, measurement, and modeled mineralogy turnaround time. This method separates the input emissivity spectrum into its constituent mineral components using a nonnegative linear least-squares fitting routine and a library of known laboratory spectral end-members (*e.g.,* Rogers and Aharonson, 2008). Given that the modeled spectrum is dependent on the spectral library used, if a mineral present in the experimental sample is not included in the spectral library, then the modeled mineralogy will not be consistent with the sample's actual mineralogy. Because of this, a large spectral library was used, with care to use multiple polymorphs for expected end-members. A total of 73 library spectral end-members, including six separate serpentine spectra, were used for this study (Supplementary Table S1; Supplementary Data are available online at www.liebertonline.com/ast). It should be noted that the spectral library will likely never contain the full range of spectral end-members within the measured sample, given the potential diversity of compositions.

2.1.2. Near-infrared. Near-infrared reflectance measurements are sensitive to a broad range of hydroxylated and hydrated mineral phases, carbonates, and Fe-bearing phases. Absorptions due to OH^- and H_2O generally occur near ~1.40 and 1.90 μm for most hydrated phases and are typically not diagnostic of a specific phase. However, metal cation-OH absorptions are present at slightly longer wavelengths (~2.10–2.40 μm), and their shape and wavelength absorption center can commonly be used to uniquely identify specific phases. For example, the reflectance spectra for the Mg-rich polymorphs of serpentine have a unique shallow 2.10–2.12 μm absorption with an asymmetric absorption centered at 2.35 μm. The identification of these absorption features in NIR reflectance spectra, in combination with the 1.40/1.90 μm OH^-/H_2O hydration absorptions, can be used to uniquely identify and distinguish the presence of serpentine from other hydrated phases (*e.g.,* Ehlmann *et al.,* 2010).

Visible and near-infrared reflectance spectra were collected at the Department of Earth and Space Sciences at the University of Washington with a portable FieldSpec4 HiRes spectroradiometer with a spectral range of 0.35–2.50 μm. Radiance was collected with a 25° full conical angle fiber-optic cable mounted to a pistol grip aimed ~2 cm from the sample. Samples were illuminated by a standard heat lamp to increase the measured signal, and stray light was limited by covering laboratory windows and acquiring measurements after sunset. Similar to the acquisition of the TIR emitted radiance, measurements were taken from multiple spots of ~2 mm^2 due to sample heterogeneity at that spatial scale (*e.g.,* Fig. 2). Data were calibrated using a spectralon calibration target, and reflectance was calculated with RS^3 Spectral Acquisition and ViewSpec Pro software.

2.2. Mars data set from the Compact Reconnaissance Imaging Spectrometer for Mars (CRISM)

CRISM is a hyperspectral visible and near-infrared imager on board the Mars Reconnaissance Orbiter with 544

spectral bands between ~0.4 and 4.0 μm (Murchie *et al.,* 2007). CRISM has multiple observation modes with several spectral and spatial samplings. The alteration phases we are interested in for this study have been identified by using full-resolution short and targeted (FRS and FRT) images with a spatial sampling of ~20 m/pixel and half-resolution short and long (HRS and HRL) images with a spatial sampling of ~40 m/pixel. For this study, we focused on examining CRISM images in locations where previous studies have identified serpentine-bearing phases, as well as other low-grade alteration phases. Furthermore, we performed automated factor analysis, similar to principal component analysis, and target transformation analyses (Malinowski, 1991; Bandfield *et al.,* 2000; Thomas and Bandfield, 2017) on all CRISM FRT, FRS, HRL, and HRS images acquired after 2011 (80 in total; see Supplementary Table S2 for list of images), as these images have not yet been described by previous studies with respect to phases associated with serpentinization. The use of factor analysis and target transformation allows for the rapid identification of the dominant spectral end-members within an image and reduces random noise. These techniques have been shown to be useful for these types of studies with CRISM data (*e.g.,* Thomas *et al.,* 2014; Thomas and Bandfield, 2017).

Although TIR measurements from the Thermal Emission Spectrometer (TES) on board the Mars Global Surveyor spacecraft have been acquired of the martian surface at high enough spectral resolutions to identify serpentine, and related phases, the spatial footprint for a single measurement taken by this instrument is approximately 3×6 km. The surface exposures in Nili Fossae of interest are significantly smaller than can be resolved with TES data. Because of this, the present study focused exclusively on CRISM NIR reflectance measurements.

CRISM images were corrected for atmospheric gas absorptions by using the scaled volcano-scan method described by McGuire *et al.* (2009) with additional atmospheric correction techniques adapted from the current CRISM Analysis Tool (CAT) v.7.2.1. Spectral index maps were created in a manner similar to that described by Pelkey *et al.* (2007) and Viviano-Beck *et al.* (2014). Spectral indices map the strength of specific spectral features that are indicative of particular phases across a CRISM image, allowing for the rapid analysis of the data. Areas of interest within a given image were then further investigated by evaluating I/F (the radiance observed by the CRISM detector divided by the solar irradiance at the top of the martian atmosphere and is equivalent to reflectance) spectra and spectral ratios to confirm the presence or absence of the spectral feature (or features) of interest. Spectral ratios were created by taking a pixel average of I/F values for an area of interest and dividing it by the I/F average for a region considered spectrally neutral (or spectrally known) within the same image columns, to reduce the effects of image striping on the spectral ratios.

3. Measurements and Observations

3.1. Lost City Hydrothermal Field measurements

3.1.1. Thermal-infrared measured emissivity. Measured TIR emissivity spectra for the Lost City samples show well-defined absorption features consistent with the basic bulk mineralogy for most of the samples and clearly separate the previously defined rock types from one another (Figs. 3–5). Most spectra indicate a mixed mineralogy, with multiple phases present.

"Carbonate" rock type spectra show a broad absorption with an emissivity minimum near 262 cm^{-1} (~38.2 μm), a distinct narrow absorption at 864 cm^{-1} (~11.6 μm), and a broad and flat-bottomed absorption near 1512 cm^{-1} (~8.7 μm). This spectral shape is most consistent with a rock dominated by aragonite based on the shapes of the measured 1512 and 262 cm^{-1} absorptions (Fig. 3). The "pelagic top-layer" rock type has low signal-to-noise emissivity spectra due to the low thermal conductivity of the fine-grained porous samples. Samples show weak absorptions near 320 cm^{-1} (~31.3 μm) and a weak,

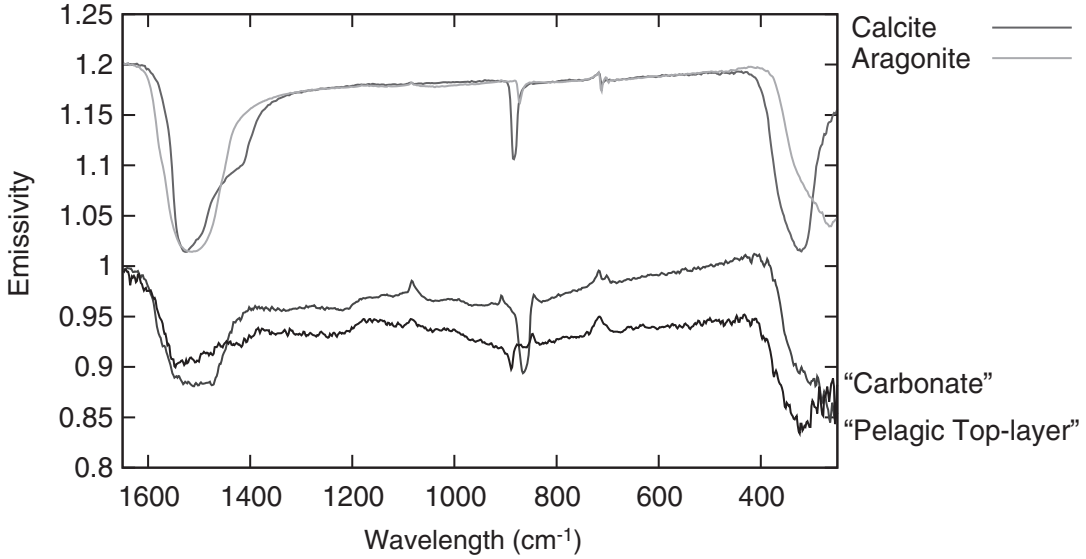

FIG. 3. Thermal-infrared emissivity measurement for "carbonate" and "pelagic top-layer" samples compared to end-member library spectra for calcite and aragonite. "Carbonate" measurements match best with library calcite spectra, while "pelagic top-layer" measurements match best with library aragonite spectra.

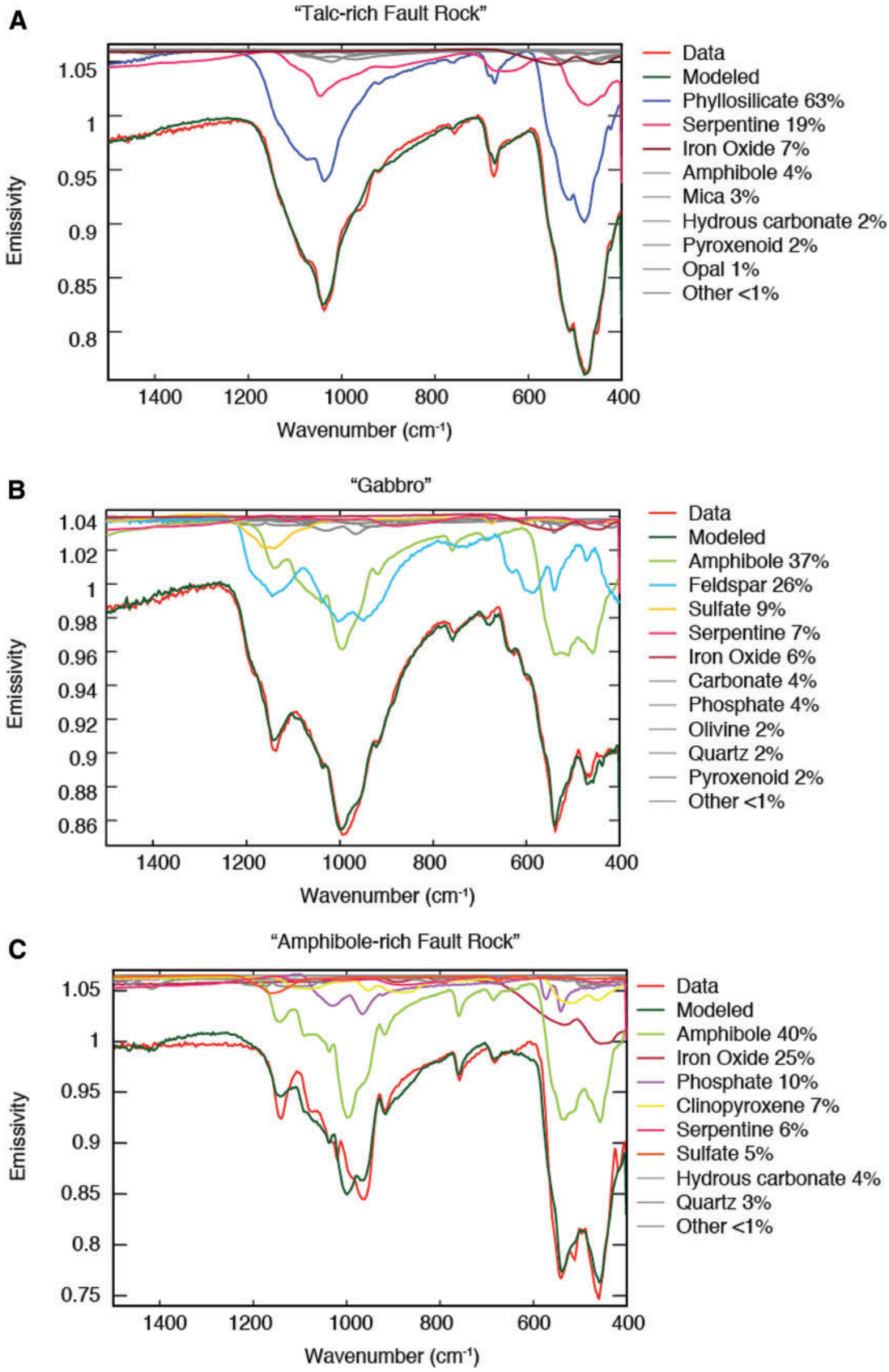

FIG. 4. Deconvolution results for non-''serpentinite'' Lost City samples. Any mineral group with abundances calculated to less than 5% have been grayed out. Spectra shown for each rock type are representative of the multiple spectra measured for each rock.

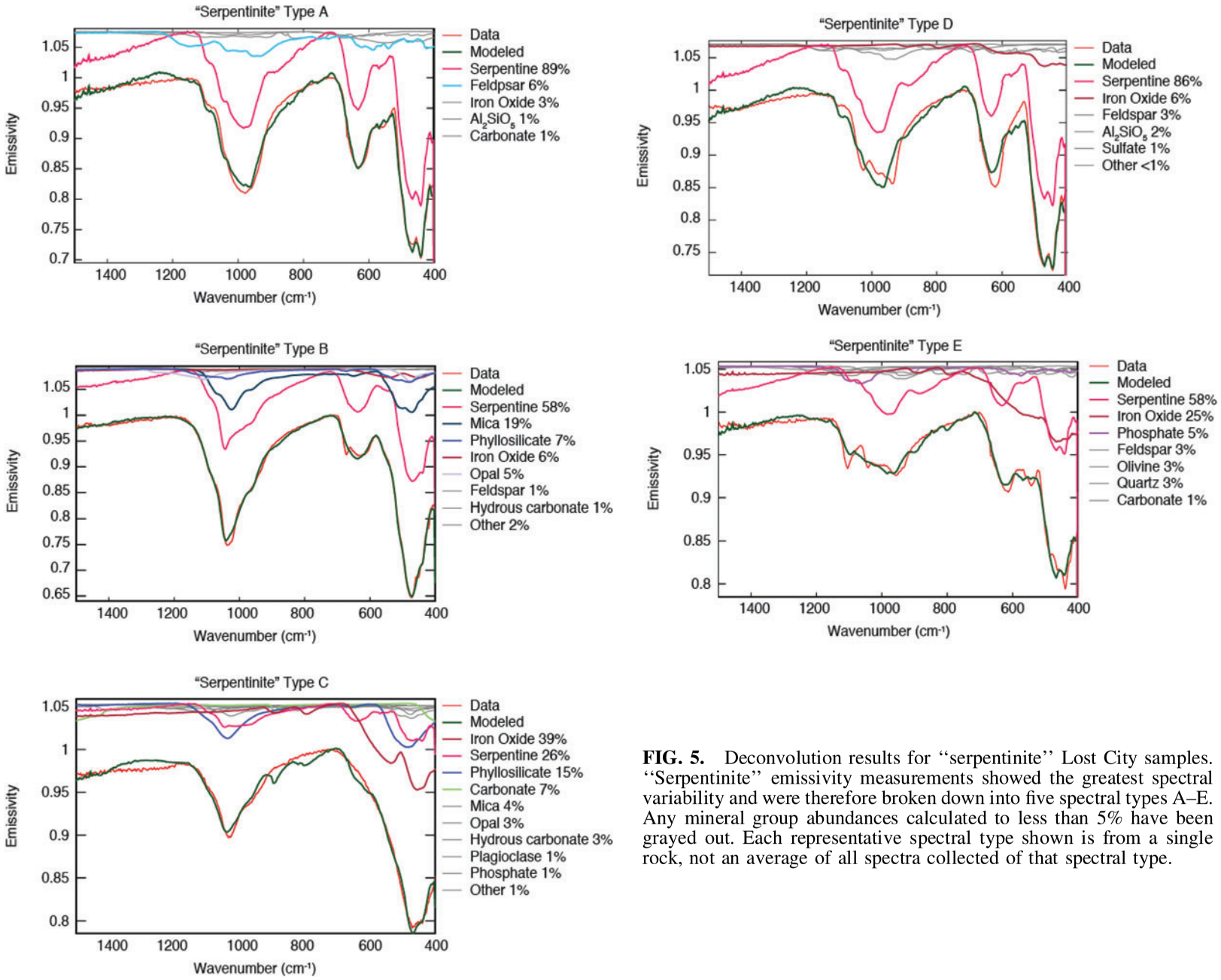

FIG. 5. Deconvolution results for ''serpentinite'' Lost City samples. ''Serpentinite'' emissivity measurements showed the greatest spectral variability and were therefore broken down into five spectral types A–E. Any mineral group abundances calculated to less than 5% have been grayed out. Each representative spectral type shown is from a single rock, not an average of all spectra collected of that spectral type.

narrow absorption near 886 cm^{-1} (~11.2 μm). These absorptions are more consistent with calcite compared to the other carbonate phases within our spectral library (*e.g.,* magnesite, dolomite) (Fig. 3).

Emissivity spectra for the ''talc-rich fault rock'' have three apparent absorptions with minima at 1035, 673, and 467 cm^{-1} (~9.6, 14.8, 21.4 μm). This spectrum is similar to laboratory spectra of talc, with the exception of the 1035 cm^{-1} absorption. Talc has an emissivity minimum shifted to longer wavenumbers, 1062 cm^{-1}, consistent with a mixed end-member spectrum (Fig. 4A). ''Gabbro'' rock–type spectra (*e.g.,* Sample #2) show two broad absorptions, one centered near 1071 cm^{-1} (~9.3 μm) and the other centered near 492 cm^{-1} (~20.3 μm), broadly consistent with amphibole and feldspar phases (Fig. 4B).

Emissivity spectra for the ''amphibole-rich fault rock'' type show two broad absorptions and two minor absorptions. A broad asymmetric absorption occurs at high wavenumbers, with an emissivity minimum of ~996 cm^{-1} (10.0 μm), two minor absorptions at 757 and 684 cm^{-1} (~13.2 and 14.6 μm), and a broad absorption with an emissivity minimum at 529 cm^{-1} (18.9 μm). The emissivity spectrum for the ''amphibole-rich fault rock'' closely matches tremolite spectra from our library (Fig. 4C).

Lost City ''serpentinite'' rock types show the most TIR spectral variability. Five different spectral types are distinguished across the five different ''serpentinite'' rock samples (Fig. 5). Samples #1, 6, 8, and 9 show ''serpentinite'' spectral type A, which has three broad absorptions centered near 978 cm^{-1} (~10.2 μm), 632 cm^{-1} (~15.8 μm), and 455 cm^{-1} (~22.0 μm). Different surfaces of Sample #4 show spectral types B and C. Type B has three dominant absorptions, a narrow absorption near 1035 cm^{-1} (~9.7 μm), a minor absorption near 641 cm^{-1} (~15.6 μm), and a deep absorption near 471 cm^{-1} (~21.23 μm). Type C has two dominant absorptions, one near 1031 cm^{-1} (~9.7 μm) and the other near 455 cm^{-1} (~22.0 μm). Only Sample #8 shows spectral type D, with three major absorptions: the first, a wide absorption centered near 983 cm^{-1} (~10.2 μm), followed by two narrow absorptions near 620 and 455 cm^{-1} (~16.1 and 22.0 μm). Lastly, Sample #9 shows spectral type E with a broad, flat-bottomed absorption near 1017 cm^{-1} (~9.8 μm) and three absorptions near 616, 540, and 455 cm^{-1} (~16.2, 18.5, and 22.0 μm). This variability in ''serpentinite''-type rocks may be attributed in particular to mineralogical heterogeneity at the scale of the spectrometer's field of view (~1 cm^2). The ''serpentinite'' rocks are characterized by large veins of differing composition, gradational alteration, and variable textures (Table 1 and Fig. 2). All measurements show absorptions consistent with the presence of serpentine phases with only minor differences from the serpentine end-members in our spectral library.

3.1.2. Thermal-infrared deconvolution modeling of mineral abundances. Thermal-infrared deconvolution modeling was performed to determine mineral abundances for appropriate emissivity spectra. Deconvolution modeling was not performed on the ''carbonate'' or ''pelagic top-layer'' rocks because they were fine-grained and porous. Fine-particulate surfaces can create particle size effects in TIR emissivity spectra that cannot be modeled by using the linear deconvolution model and therefore do not produce quantitatively useful mineral abundances (*e.g.,* Lyon, 1965; Ramsey and Christensen, 1998; Lane, 1999). However, their apparent absorptions allow for qualitative comparison to spectral library end-member samples, and the emissivity spectra can still be used to identify major phases. ''Carbonate'' rocks are clearly dominated by aragonite (Fig. 3) as the shape and emissivity minimum for the low and high wavenumber absorptions match those of aragonite library spectra. Likewise, ''pelagic top-layer'' rocks are dominated by calcite (Fig. 3).

All other TIR emission spectra were suitable for linear deconvolution modeling to determine quantitative bulk-rock mineral abundances. There are two different approaches to looking at these results. First, the results can be viewed in terms of the dominant contributing mineral *groups* (*e.g.,* feldspar, amphibole, phyllosilicate) (Figs. 4–5) for a given spectrum. For this study, serpentine phases (*e.g.,* antigorite, chrysotile, and lizardite) have been separated from the phyllosilicate group and are their own stand-alone serpentine mineral group.

The data can also be viewed in terms of individual end-member abundances (Table 2). To an extent, this allows us to understand what particular phases are contributing to the mineral group abundances observed (*e.g.,* whether lizardite or antigorite is the dominant phase contributing to the serpentine group abundance for a particular rock sample). In general, the discriminability between mineral phases under optimal conditions is between 5 and 7 vol % (Ramsey and Christensen, 1998); however, associated errors and the model's ability to discriminate between mineral phases are impeded when spectral end-members have shallow, nondescript absorptions and/or when phases have similar spectral shapes. The model's ability to distinguish end-members within a given group is less than that of distinguishing between the different groups themselves, but these quantitative results still provide a first-order look into what particular phases are likely contributing to the rock's spectrum.

In general, the deconvolution modeling of measured spectra show that the Lost City rock samples include variable mineralogy but that they are typically dominated by one to two phases. The dominant end-member spectra for the non-carbonate samples are serpentine, tremolite (amphibole), labradorite (feldspar), and talc (Figs. 4–5 and Table 2). Mineral deconvolution results are typically in agreement with the rock types identified by previous studies (*e.g.,* Karson *et al.,* 2006; Boschi *et al.,* 2006; Delacour *et al.,* 2008).

Deconvolution results for the ''talc-rich fault rocks'' generally match previous descriptions of the samples, (*i.e.,* a mixture of serpentine, talc, and amphibole Karson *et al.,* 2006; Boschi *et al.,* 2006]). Mineral deconvolution shows that the measured spectra can be modeled by ~63 vol % phyllosilicate (excluding serpentine phases) and ~19 vol % serpentine phases, with nearly equal spectral contributions from all three polymorphs (Table 2). Talc and saponite are the largest phyllosilicate contributors with approximately 42 vol % talc and 21 vol % saponite. Karson *et al.* (2006) described this sample as a ''serpentinite/talc-amph schist'' (Table 1); however, the deconvolution results did not include amphibole as a dominant contributor within our detection limits, though all other dominant end-members were confirmed.

Similarly, deconvolution modeling of the ''gabbro''-type rocks had good fits with the measured emissivity spectra. These spectra are dominated by feldspar (specifically in the form of labradorite) and amphibole (in the form of tremolite and hornblende); this is consistent with metamorphic alteration

Table 2. Thermal-Infrared Deconvolution Model Results for the Non-Carbonate Rocks Used for This Study

		Talc-rich fault rock	*Gabbro*	*Amphibole-rich fault rock*	*Serp A*	*Serp B*	*Serp C*	*Serp D*	*Serp E*
Group	*End-member*	*Normalized abundance (%) for abundances above 4% detection limit*							
Serpentine	Antigorite	6.08	—	—	43.09	6.3	22.38	31.02	14.98
	Chrysotile	6.98	7.22	6.08	—	7.54	—	—	
	Lizardite	5.98	—	—	45.46	44.66	—	55.03	40.48
Phyllosilicate	Talc	41.87	—	—	—	—	—	—	
	Saponite	20.64	—	—	—	—	12.43	—	
Iron Oxide	Ilmenite	—	—	—	—	—	—	—	7.94
	Hematite	6.9	—	12.97	—	5.44	26.55	—	5.84
	Goethite	—	6.03	7.94	—	—	12.78	—	10.72
Feldspar	Labradorite	—	24.44	—	—	—	—	—	
	Anorthite	—	—	—	4.57	—	—	—	
Amphibole	Tremolite	—	17.27	26.08	—	—	—	—	
	Hornblende	—	11.01	—	—	—	—	—	
	Anthophyllite	—	5.43	—	—	—	—	—	
	Actinolite		—	11.73	—	—	—	—	
Sulfate	Gypsum	—	6.9	4.56	—	—	—	—	
Phosphate	Pyromorphite	—	—	9.88	—	—	—	—	
Clinopyroxene	Hedenbergite	—	—	7.05	—	—	—	—	
Mica	Chlorite	—	—	—	—	9.58	—	—	
	Biotite	—	—	—	—	9.38	—	—	
Opal	Opal-CT	—	—	—	—	5.26	—	—	
Carbonate	Dolomite	—	—	—	—	—	6.5	—	

of the original gabbroic rock (Fig. 4B, Table 2). The ''gabbro'' spectrum also has minor spectral contributions from chrysotile ($\sim$7 vol %) (Table 2). The estimated 9 vol % sulfate may also be consistent with the observations of sulfate in Lost City hydrothermal fluids (Kelley *et al.,* 2005) and sulfur found in underlying mantle rocks (Delacour *et al.,* 2008).

The ''amphibole-rich fault rock'' spectra were indeed dominated by 40 vol % amphibole phases, primarily in the form of tremolite and actinolite. The modeled spectrum has significant contributions from iron oxide phases ($\sim$25 vol %) and pyroxene and phosphate phases ($\sim$7 and 10 vol %, respectively). However, the model fit to the measured emissivity spectra was not ideal, especially for the broad asymmetric absorption near 996 cm^{-1} ($\sim$10.0 μm), implying that our spectral library is somewhat incomplete and does not contain all specific phases present within this sample. The overall shape of this absorption is consistent with tremolite emissivity spectra, but the measured spectrum is shifted to slightly lower wavenumbers (Fig. 4C).

Lastly, the deconvolution results for the ''serpentinite'' samples show that all samples were dominated by serpentine phases but have variability in terms of the specific serpentine phases present and other mineral contributors (Fig. 5). The modeled fit for ''serpentinite'' Type A spectrum is composed of $\sim$89 vol % serpentine, with nearly equal contributions from lizardite and antigorite end-member spectra. ''Serpentinite'' Type B modeled spectrum is composed of 58 vol % serpentine, mostly in the form of lizardite, but with minor contributions from both chrysotile and antigorite, and $\sim$20 vol % mica. Spectral type C for the ''serpentinite'' samples shows an elevated abundance of iron oxides ($\sim$39 vol %) in the modeled spectrum. Serpentine is the second largest mineral group contributor, with a modeled abundance of $\sim$25 vol %, mostly in the form of antigorite. Lastly, deconvolution results show $\sim$12 vol % saponite (phyllosilicate group). Deconvolution results for ''serpentinite'' spectral type D show $\sim$86 vol % serpentine, primarily composed of lizardite and antigorite ($\sim$55 and $\sim$31 vol %, respectively). The modeled fit lacks the fine spectral structure in the measured spectrum within the broad 1000 cm^{-1} ($\sim$10.0 μm) absorption but fits well at lower wavenumbers near $\sim$450 cm^{-1} ($\sim$22.2 μm) and with the overall shape of the measured spectrum. Lastly, the modeled spectrum for ''serpentinite'' spectra Type E is composed of 58 vol % serpentine in the form of lizardite and antigorite ($\sim$40 and $\sim$15 vol %, respectively) and $\sim$25 vol % iron oxides. In this case, the modeled spectrum has minor spectral features that are not present in the measured spectrum but matches well with the overall shape of the measured spectrum.

Overall, the measured emissivity spectra for the Lost City rocks are consistent with the bulk-rock compositions for these samples. In addition, the deconvolution modeling showed the range of phases within a given rock type. For example, serpentine phases were found within all the silicate rock-types. Specifically, when serpentine phases were present in deconvolution results for the non-''serpentinite'' rock types (*i.e.,* the ''talc-rich fault rock,'' ''amphibole-rich fault rock,'' and the ''gabbro''), they typically contained a higher concentration of chrysotile (Table 2). The ''serpentinite'' rock types were predominately composed of lizardite followed by antigorite. In addition, the ''gabbro'' would be better defined as a metagabbro given its alteration mineralogy. See Section 4.1.3 for detailed discussion of mineral results with respect to phases expected from theoretical serpentinization reaction (Reactions 1–3).

3.1.3. Near-infrared measured reflectance. Near-infrared reflectance spectra of the bedrock Lost City samples show absorptions typical of ultramafic and mafic rock types and minerals associated with serpentinization. All spectra show clear 1.4 and 1.9 μm absorptions indicative of either structurally bound or adsorbed OH^- and H_2O (Fig. 6).

Reflectance spectra for the ''carbonate'' and ''pelagic top-layer'' samples also show 1.4 and 1.9 μm hydration absorptions, a broad ~2.3 μm absorption, and part of an absorption centered near 2.5 μm (Fig. 6). The combination of 2.3 and 2.5 μm absorptions are overtones and combinations due to C-O stretching and bending fundamental crystal lattice vibrations in carbonates (*e.g.,* Gaffey, 1987). The wavelength minima of the 2.5 μm absorption can typically be used to identify the specific major metal cation (*e.g.,* Mg or Ca), but given that this absorption is not fully sampled by the spectral range of the laboratory spectrometer, we are unable to identify the associated cation from these spectra alone. However, our TIR spectral analysis (Section 3.1.1), as well as previous studies, identifies these samples as dominated by aragonite and calcite (Ca carbonates) (Fig. 3).

Near-infrared reflectance spectra measured for the ''talc-rich fault rock,'' ''amphibole-rich fault rock,'' and the ''gabbro'' show similar spectral absorptions with only minor differences (Fig. 6). The ''talc-rich fault rock'' has the deepest absorptions (highest spectral contrast) compared to the other two phases. Reflectance spectra for this sample, a compositional mixture dominated by serpentine, talc, and saponite, as confirmed by the TIR measurements and analysis, show a weak 2.1 μm absorption (consistent with serpentine) and two longer-wavelength absorptions at 2.31 and 2.38 μm. The latter two absorptions can be attributed to talc, saponite, or amphibole (*e.g.,* actinolite and/or tremolite), as these phases are difficult to distinguish spectrally at these wavelengths (*e.g.,* Brown *et al.,* 2010; Viviano *et al.,* 2013) (Fig. 7). However, the analysis of the TIR spectra confirms the presence of both talc and saponite phases in the ''talc-rich fault rock'' with small amounts of amphibole.

Both the ''amphibole-rich fault rock'' and the ''gabbro'' samples show the same two long-wavelength absorptions near 2.31 and 2.38 μm as the ''talc-rich fault rock'' (Fig. 6). Library spectra for amphibole (*e.g.,* tremolite) reflectance measurements show that these two absorptions would also be expected for these amphibole group phases (Fig. 7). The reflectance spectra for these three rock types look extremely similar in the NIR wavelength region. Without the confirmation of bulk mineralogy derived from the TIR measurements, they would be difficult to distinguish.

Rocks that were described as ''serpentinites'' in previous works, and confirmed as such by TIR emissivity analysis, show diagnostic absorptions associated with Mg-serpentine phases (*i.e.,* lizardite, antigorite, and chrysotile) in their reflectance spectra. A unique 2.10–2.12 μm absorption in association with a sharp, asymmetric 2.33 μm Mg-OH combination band clearly indicates the presence of serpentine phases (Fig. 6). Mg-serpentine phases also typically have a 2.52 μm absorption, but given the limited spectral range of the measurements, this absorption could not be fully characterized for these samples. A negative slope in the reflectance at wavelengths >2.45 μm is present and likely due to this expected absorption.

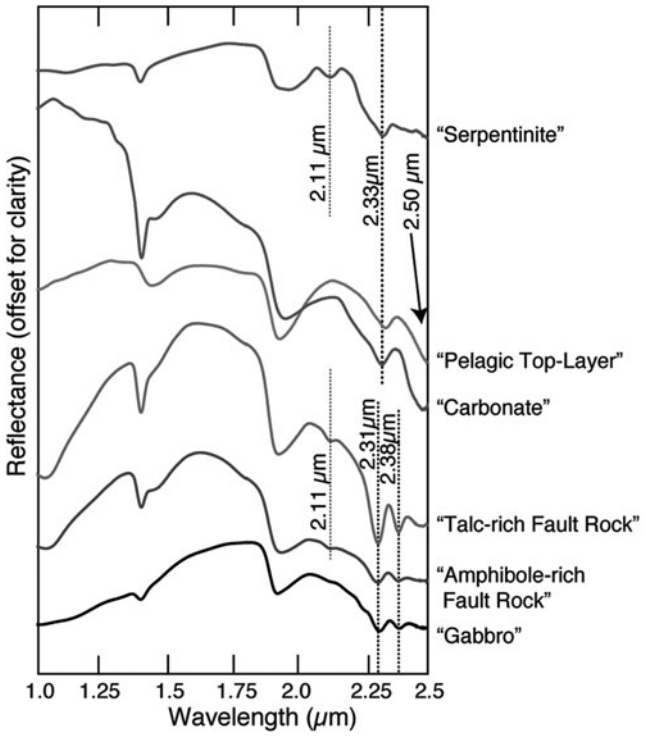

FIG. 6. Near-infrared reflectance measurements for Lost City rock samples.

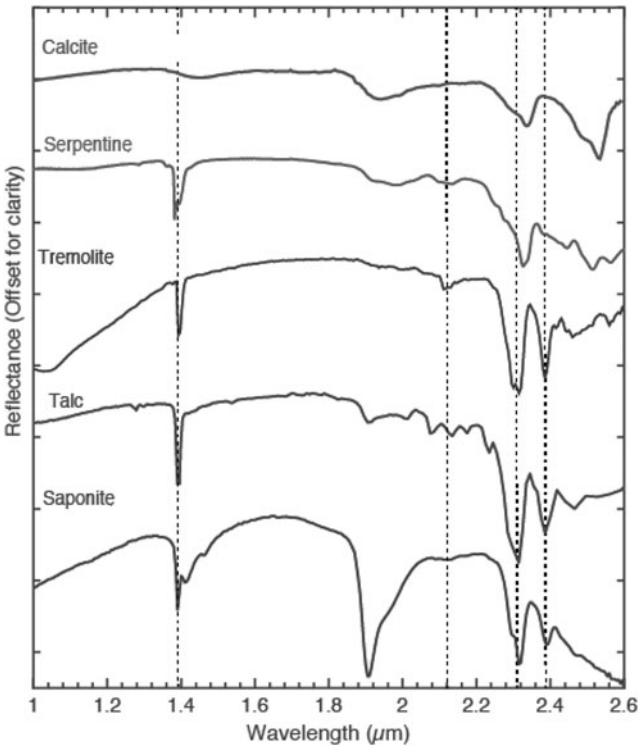

FIG. 7. Near-infrared library spectra for serpentine, tremolite (amphibole), talc, and saponite. Serpentine can be uniquely identified by an absorption ~2.1 μm. Amphibole, talc, and saponite are difficult to distinguish spectrally in this wavelength region.

3.2. Mars observations: Low-temperature serpentinization mineral assemblage in Nili Fossae, Mars

In the present study, we aggregated all observations of mineral phases in Nili Fossae associated with low-temperature serpentinization processes on Earth (Fig. 8). Previous studies have documented the presence of olivine-rich basalts (Hoefen *et al.,* 2003; Hamilton and Christensen, 2005), carbonates (Ehlmann *et al.,* 2008; Thomas and Bandfield, 2017), and three low-grade metamorphic alteration mineral phases: serpentine, talc, and/or saponite (Ehlmann *et al.,* 2009, 2010; Brown *et al.,* 2010; Viviano *et al.,* 2013). We also included additional observations of serpentine, talc/saponite, and Mg carbonate using automated factor analysis and target transformation techniques (Thomas and Bandfield, 2017) (Supplementary Table S3). The following section describes where these phases are observed and their diagnostic spectral characteristics at NIR wavelengths, and these spectral observations will be directly compared with Lost City NIR measurements.

Olivine: Serpentine, talc/saponite, and Mg carbonates have been identified in regional proximity with an extensive olivine-rich basalt unit (*e.g.,* Ehlmann *et al.,* 2009; Viviano *et al.,* 2013). The largest exposures of the olivine-rich basalt span an approximately $150 \times 300\,km^2$ region to the northeast of the Nili Fossae troughs, though smaller exposures are observed to the west and south of the main troughs. Quantitative deconvolution analyses of emission spectra from the Mars Global Surveyor TES data indicate that this olivine-rich basalt unit contains between 20 and 30 wt % olivine with compositions ranging from Fo_{68} to Fo_{75}, indicating a Mg-rich olivine end-member (Hoefen *et al.,* 2003; Hamilton and Christensen, 2005; Koeppen and Hamilton, 2008; Edwards and Ehlmann, 2015).

The Mg content of the olivine is also confirmed by NIR spectral data from the OMEGA (Observatoire pour la Minéralogie, l'Eau, les Glaces et l'Activité; Bibring *et al.,* 2004) and the CRISM instruments (*e.g.,* Ody *et al.,* 2013). CRISM ratioed I/F spectra for this unit show a broad absorption between $\sim$1.1 and 1.9 µm due to the ferrous component of olivine, typical of an olivine-rich basalt (Fig. 9).

Carbonates: Mg-carbonate spectral signatures have been observed within some exposures of the olivine-rich basalts and occupy the same stratigraphic unit as the olivine (*e.g.,* Ehlmann *et al.,* 2008). CRISM ratioed I/F spectra for these exposures include a broad 1.10–1.85 µm absorption consistent with the presence of olivine, a 1.9 µm combination overtone from structural H_2O, an asymmetric narrow 2.3 µm absorption, and a broader 2.5 µm absorption (*e.g.,* Ehlmann *et al.,* 2008) (Fig. 9). The wavelength minimum for the 2.5 µm absorption is consistent with Mg carbonate (Ehlmann *et al.,* 2008).

Serpentine: Three serpentine-bearing exposures have been identified in the region, two by Ehlmann *et al.* (2009) and one by authors of the present study (CRISM FRT0002AE17_01). As for the Mg-carbonate exposures, these exposures are found within the olivine-rich stratigraphic unit. CRISM

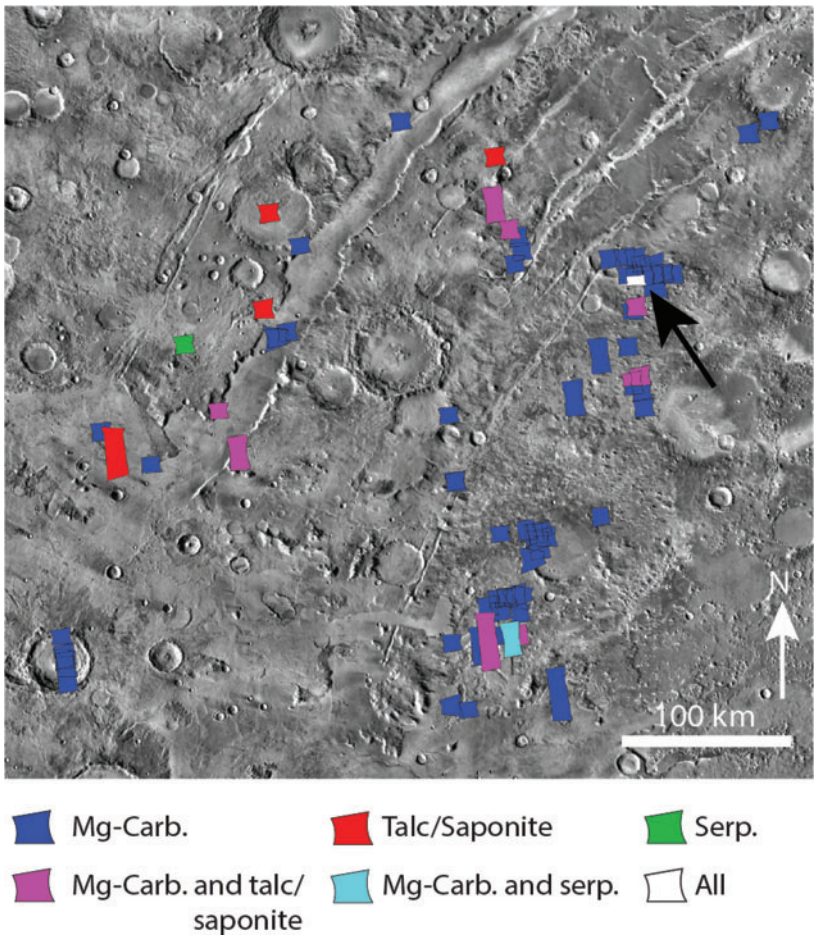

FIG. 8. Alteration mineral distribution map for Nili Fossae on THEMIS Global Day IR mosaic background centered on 75.7°E, 20.8°N. CRISM stamp colors indicate the identification of one, or multiple, alteration phases of interest within that given CRISM image. Identifications made in the present study and by Ehlmann *et al.* (2009), Viviano *et al.* (2013), and Thomas and Bandfield (2017). Bold black arrow indicates CRISM image FRS0002AE17_01 shown in detail in Fig. 10.

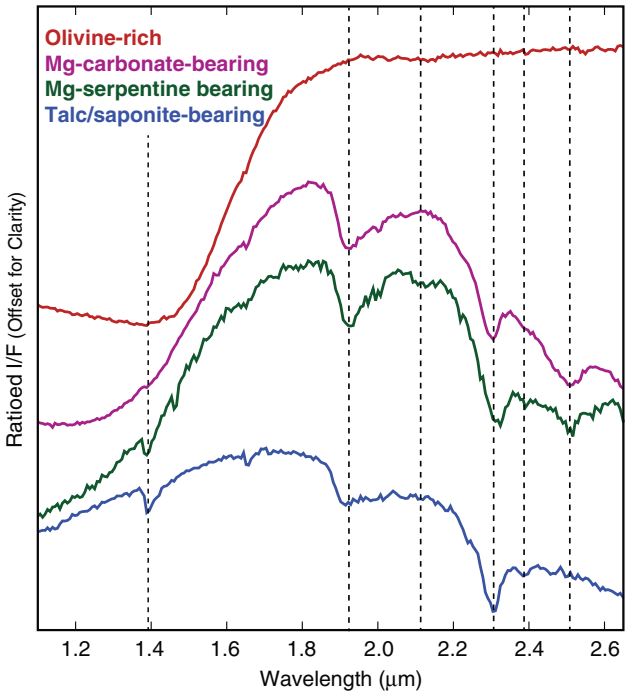

FIG. 9. CRISM ratioed I/F spectral measurements for the spectral suite associated with low-temperature serpentinization found in Nili Fossae. Olivine and Mg-carbonate spectra from CRISM image FRT00003E12_07 (Ehlmann *et al.,* 2008), Mg-serpentine spectrum from CRISM image FRT0000ABCB_07 (Ehlmann *et al.,* 2009), and talc/saponite spectrum from CRISM image FRT0000A053_07 (Viviano *et al.,* 2013). (See Table 3 for pixel locations.)

ratioed I/F spectra of serpentine-bearing surfaces contain a broad short-wavelength absorption consistent with olivine-bearing material; 1.39 and 1.90 μm absorptions consistent with hydration (bound OH^- and H_2O); and a series of longer wavelength absorptions, including a weak 2.10–2.12 μm absorption and 2.32 μm (Mg-OH), 2.38 μm, and 2.50 μm absorptions (Fig. 9). The combination of the 1.38, 2.10–2.12, 2.32, and 2.50 μm absorptions are unique to Mg-serpentine (*e.g.,* Ehlmann *et al.,* 2010). The 2.38 μm absorption is consistent with the presence of other Mg phyllosilicates, like talc and saponite—or potentially amphibole (*e.g.,* Brown *et al.,* 2004).

Talc/Saponite/(Amphibole?): Lastly, a phase consistent with talc or possibly saponite has been identified in isolated areas across the Nili Fossae region (*e.g.,* Brown *et al.,* 2010; Viviano *et al.,* 2013). These are typically found near Mg-carbonate-bearing exposures, but not necessarily co-spatially (Fig. 8). Spectra for these exposures typically contain a narrow 1.38 μm absorption, a broad asymmetric 1.90 μm OH^-/H_2O absorption, a strong narrow 2.32 μm absorption, and a weaker absorption at 2.38 μm (Fig. 9). It should be noted that, as with the NIR laboratory spectra described in Section 3.1.3, it is not possible to distinguish talc/saponite from amphiboles like tremolite or actinolite by using reflectance spectra at these wavelengths (Figs. 6 and 7). As such, it is unclear whether surfaces with these spectral characteristics represent a single phase or various combinations of these spectrally ambiguous phases.

There is one CRISM image that contains all four spectral types (olivine, serpentine, carbonate, and talc/saponite/amphibole) within a single scene: FRS0002AE17_01 (Fig. 10; Table 3). The ratioed I/F spectra for the serpentine-bearing exposures in this image show a clear absorption near 2.11 μm, in addition to absorptions near 1.90 and 2.32 μm. A phase with two absorptions, ~2.30 and ~2.40 μm, may be consistent with talc, saponite, and/or amphibole but was only weakly identified by the D2300 index, likely because its 2.32 μm absorption is relatively shallow compared to the carbonate and other Fe/Mg-smectite phases found within the image. The 2.30/2.40 μm spectral type found in this image is less consistent with a pure talc/saponite spectral end-member, which typically has wavelength absorption centers closer to 2.32 and 2.38 μm; however, this may be due to the limited spatial scale of this exposure or partial alteration leading to more complicated mineralogy.

4. Discussion

4.1. Laboratory measurements

4.1.1. Usefulness of thermal-infrared measurements. Through this nondestructive analytical method, the mineralogy of rock types from the Lost City Hydrothermal Field is in agreement with past studies and has been useful in providing a detailed description of the mineralogy. This has been particularly illuminating with the ''serpentinite'' rock types, which show considerable variability in their emissivity spectra.

Five different spectral types were documented within the ''serpentinite'' rocks. Characterization of types A and B are reproduced well with the spectral end-member library used for deconvolution modeling (Fig. 5), implying that the majority of phases present within those rock samples were also found in our spectral end-member library. Deconvolution modeling for ''serpentinite'' spectral types C, D, and E shows general agreement with the emissivity measurements for those rocks, but the modeling either added or missed minor absorptions. In these cases, the spectral end-member library was likely incomplete and did not include the full range of phases present within the rock samples.

Serpentine is a particular case where there is a great deal of expected variability both in terms of mineral phases and spectral characteristics (*e.g.,* Wicks and O'Hanley, 1988). A search for TIR emissivity spectra of lizardite, antigorite, and chrysotile across spectral libraries (*e.g.,* the U.S. Geological Survey Spectral Library [Clark *et al.,* 2007], the Arizona State University Spectral Library [Christensen *et al.,* 2000]) shows a wide range of spectral characteristics for these phases (Fig. 11), all with similar general shapes but variable detail. Similarly, our serpentinite samples, all from the same low-T hydrothermal system, show a range of observed emissivity spectra, though the overall shapes are still consistent with known serpentine spectra. Therefore, in addition to confirming that these samples are indeed serpentinites, these spectra serve as spectral end-members and demonstrate the spectral variability for this particular low-T serpentinizing environment.

4.1.2. Observed patterns in thermal-infrared measurements. Thermal-infrared emissivity measurements show several patterns of dominant Mg-serpentine polymorphs

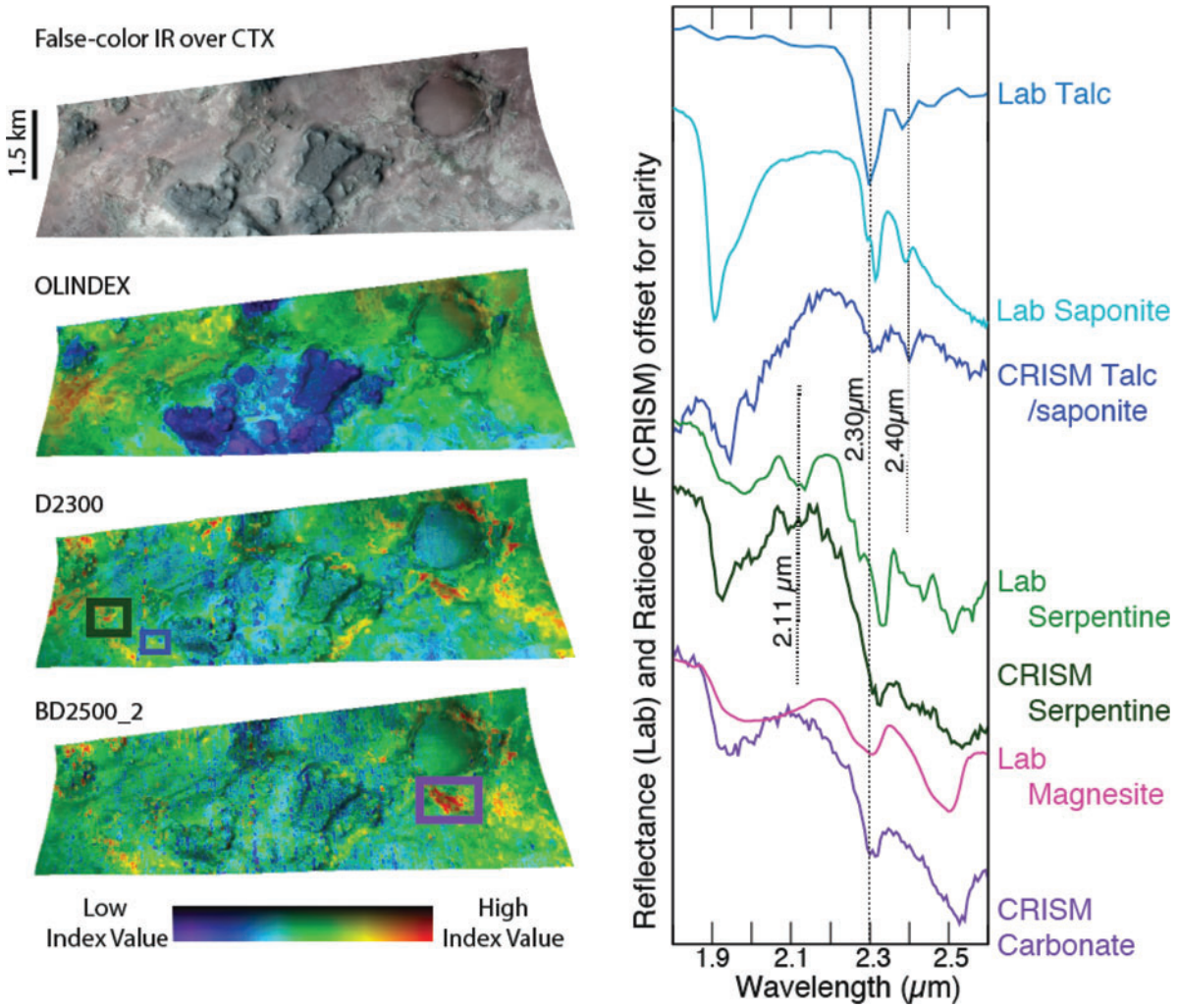

FIG. 10. CRISM image FRS0002AE17_01 (black arrow in Fig. 8) with new detections of serpentine, carbonate, and talc/saponite in association with the olivine-rich basalt unit. Note that the overall shape of the talc/saponite spectrum appears to be affected by a pyroxene phase likely due to subpixel mixing. False-color IR image projects CRISM wavelengths 2.53, 1.50, and 1.08 μm as red, green, and blue, respectively. The OLINDEX, D2300, BD2500 indices each show colorized maps indicating the intensity of spectral features associated with olivine, Fe/Mg phyllosilicates, and Mg carbonates, respectively. The green box in the D2300 index indicates the surfaces used for the CRISM serpentine-bearing spectrum shown to the right, the blue box in the D2300 index indicates the surfaces used for the CRISM talc-bearing spectrum shown to the right, and the purple box in the BD2500 index indicates the surfaces used for the CRISM Mg-carbonate-bearing spectrum shown to the right. See Table 3 for exact CRISM pixel locations for displayed spectra.

within the different Lost City rock samples. The three Mg-rich serpentine polymorphs are lizardite, chrysotile, and antigorite. Lizardite is expected to form in low-temperature serpentinizing environments where fluid temperatures are typically between 50°C and 300°C, and the typical co-products are magnetite and H_2 (+/− brucite) (Evans, 2004, 2010). Consistent with the low-temperature regime that they form in, the predominate serpentine polymorph in the Lost City ''serpentinites'' is lizardite, apart from serpentine spectral type C.

Table 3. CRISM Sample and Line Numbers for Spectra Shown in Figures 9 and 10

Figure Number	*CRISM Image ID*	*Label*	*Numerator (column; row)*	*Denominator (column; row)*
9	FRT00003E12_07	Olivine-rich	(133–137; 274–278)	(133–137; 258–262)
		Mg-carbonate-bearing	(136–140; 103–107)	(136–140; 211–215)
	FRT0000ABCB_07	Mg-serpentine-bearing	(253–257; 60–62)	(253–257; 17)
	FRT0000A053_07	Talc/saponite-bearing	(104–108; 409–413)	(104–108; 416–421)
10	FRS0002AE17_01	CRISM talc	(151–156; 175–181)	(151–156; 155–147)
		CRISM serpentine	(79–82; 129–131)	(79–82; 142–143)
		CRISM carbonate	(489–497; 120–126)	(489–497; 107–113)

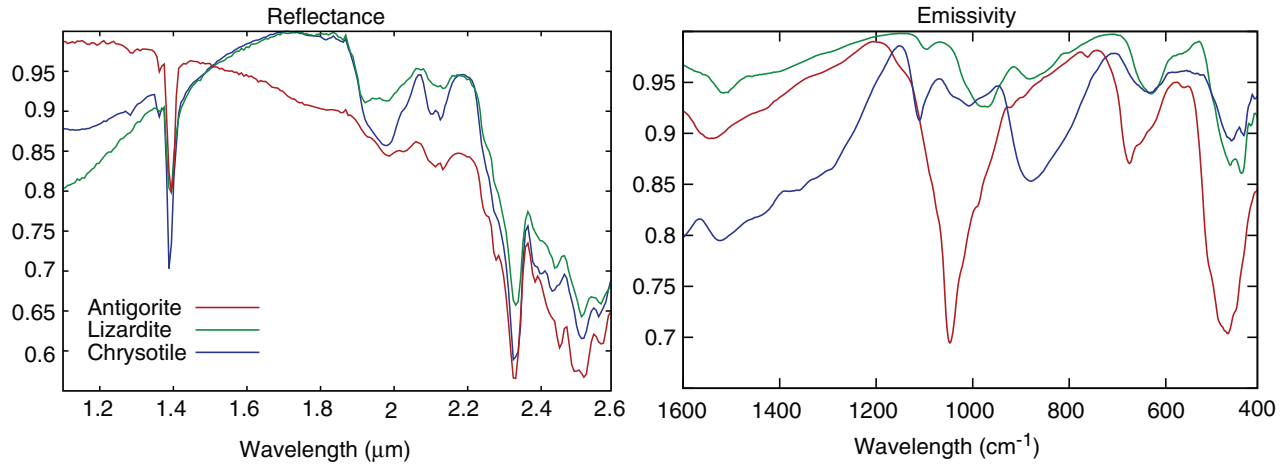

FIG. 11. Near-infrared reflectance and thermal-infrared emissivity spectra for the three Mg-rich serpentine polymorphs. The polymorphs have nearly indistinguishable spectral absorptions in the near-infrared while having unique spectral shapes and contrast in the thermal-infrared.

Similar to lizardite, chrysotile growth is favored at low fluid temperatures but typically under isotropic stress at the micro scale; this generally begins after the active hydration of olivine has ended (Evans, 2004). Hence, lizardite is the initial stable form of serpentine in low-temperature serpentinizing regimes but is typically recrystallized to chrysotile when under stress, as in a tectonically active setting (*e.g.,* Boschi *et al.,* 2006; Denny *et al.,* 2016). Again, consistent with their tectonic and alteration history, chrysotile is typically the predominant serpentine phase in the fault rocks and metagabbro, as those rocks presumably underwent extensive tectonic stress and deformation. These results are consistent with past studies (*e.g.,* Boschi *et al.,* 2006).

Lastly, antigorite typically forms at temperatures >250°C with brucite, when rates of MgFe diffusion in olivine are orders of magnitude faster than in the low-temperature systems, such as in mantle fore-arc wedges (Evans, 2004, 2010). These increased reaction rates limit the amount of magnetite and H_2 produced (Evans, 2004). We observe modeled antigorite in several ''serpentinite'' spectral types in the Lost City samples; however, they are never the predominant serpentine polymorph. The absence of significant antigorite has been described by others who have studied these rocks previously (*e.g.,* Früh-Green *et al.,* 2004).

4.1.3. Observed phases compared to theoretical serpentinization reactions. Our deconvolution results of TIR emissivity measurements are generally in agreement with expected mineral phases from theoretical serpentinization reactions (Reactions 1–3). However, notably missing from our derived mineralogy are brucite (Mg hydroxide) and magnetite (Fe oxide). Both phases were included in our end-member spectral library, but neither was modeled in the deconvolution results. There are several reasons why those phases might not be reflected in the modeled mineralogy. Magnetite has high emissivity values in the TIR with shallow absorptions near 600 and 300 cm^{-1}. As such, it is difficult to detect magnetite with this technique. Conversely, brucite has distinct spectral absorptions in the TIR. Brucite in previous studies was found within the carbonate-bearing rocks (Ludwig *et al.,* 2006), but we were unable to use the deconvolution model to determine mineral abundances for these samples due to textural effects.

Deconvolution models of the Lost City rock samples indicate significant talc. Though not a direct product of serpentinization, talc-rich rocks are commonly found in association with serpentinites and are present within the Lost City highly metasomatized ultramafic rocks (*e.g.,* Früh-Green *et al.,* 2004). On Earth, the most abundant occurrence of talc is in metamorphosed ultramafic rocks (Evans and Guggenheim, 1988), similar to what is observed at Lost City. Talc forms as a product of the alteration of serpentine by dissolved silica (*e.g.,* Moore and Rymer, 2007) and tends to break down at ~800°C (Evans and Guggenheim, 1988). A recently discovered talc-dominated hydrothermal system off the Mid-Cayman Spreading Center also informs about the generation of this mineral in mafic to ultramafic environments (Hodgkinson *et al.,* 2015).

4.1.4. Near-infrared spectral ambiguity. A notable difference between the NIR and TIR measurements is their ability to distinguish between the different rock types and the spectral variability within a given rock type. For example, the ''serpentinite'' rock types show five different spectral types in the TIR (Fig. 5), all consistent with a serpentine-rich rock, but with notable variability. The five ''serpentinite'' rocks measured in the NIR have consistent spectral absorptions with limited variability; the serpentine spectrum in Fig. 6 is representative of all NIR measurements for ''serpentinite'' rocks. The three Mg-serpentine polymorphs that make up the ''serpentinite'' rocks are distinguishable and identifiable in the TIR but appear spectrally ambiguous in the NIR portion of the spectrum. King and Clark (1989) showed that some distinctions between Mg-serpentine polymorphs can be made from the exact wavelength center and shape of the relatively weak 1.4 μm OH^- absorption, when samples are pure. Our work further demonstrates the importance of having both measurements to properly characterize the suite of minerals within this set of bulk-rock samples.

Similarly, the ''talc-rich fault rock,'' ''amphibole-rich fault rock,'' and the ''gabbro'' have nearly identical spectral

characteristics in the NIR portion of the spectrum. Talc and amphibole are known to contain similar, deep spectral absorptions in the NIR portion of the spectrum (Fig. 7). In the case of the ''gabbro,'' the observed absorptions are likely due to the ~35 vol % amphibole and serpentine phases modeled in the rock composition (Table 2). The TIR emissivity measurements were used to determine the specific composition for these three rock types, and the NIR measurements indicate the presence of H_2O/OH^- and OH^- stretch and Mg-OH^- bending modes (*e.g.,* in Mg phyllosilicates or from hydroxyl in amphiboles).

4.2. Mars observations: Compositions as described by CRISM

As presented by past studies, the mineral assemblages detected in Nili Fossae are consistent with low-temperature hydrothermal alteration of an ultramafic protolith (*e.g.,* Viviano *et al.,* 2013). In particular, the spectral detection of phases consistent with serpentine and magnesite are unambiguous and clearly indicate their presence within the rock record in Nili Fossae. The detection of a phase with absorptions near 1.4, 1.9, 2.3, and 2.4 μm (Figs. 9 and 10) has been attributed to the Mg-rich smectite saponite (*e.g.,* Ehlmann *et al.,* 2009; Brown *et al.,* 2010) and to talc (*e.g.,* Brown *et al.,* 2010; Viviano *et al.,* 2013). As we have shown in earlier sections, talc, saponite, hydroxylated/hydrated amphibole are spectrally ambiguous in the NIR portion of the spectrum (Fig. 7). Viviano *et al.* (2013) argued that talc and saponite are not spectrally ambiguous and that it is possible to differentiate the two phases based on the shape and spectral contrast of the 2.3/2.4 μm absorptions, and they argued that the surfaces in question in Nili Fossae are talc-bearing. Viviano *et al.* (2013) also argued that the presence of talc is consistent within the greater mineralogical context of the region in that it can form through the carbonation of serpentine to form talc and magnesite (*e.g.,* Viviano *et al.,* 2013).

Despite this spectral conundrum, the spectral ambiguities observed in Nili Fossae are similar to those in the Lost City rocks. Mg-rich saponite typically forms via the hydrothermal alteration of basalt (Evans and Guggenheim, 1988). Given that olivine-poor basalt is regionally abundant in Nili Fossae within the same stratigraphic column as the observed talc/saponite exposures, it is possible that saponite formation could occur. In addition, talc and saponite have been shown to form within mixed-layered structures at submarine hydrothermal sites on Earth (Cuadros *et al.,* 2008; Michalski *et al.,* 2015), making their spectral disambiguation even more difficult and showing that the two phases do form together. Similarly, our analyses of Lost City rock samples show that talc and saponite can both be significant constituents of rocks that form in serpentinizing systems as is the case with the ''talc-rich fault rock'' (Table 2). So while the distinction of whether this spectral signature in Nili Fossae is due to talc or saponite has specific implications for the alteration trajectory of these rocks, we have shown that these phases are not mutually exclusive and are both well represented within low-temperature serpentinizing systems on Earth.

Lastly, it is important to note that, with the CRISM NIR data alone, it is not possible to determine whether the ambiguous 1.4/1.9/2.3/2.4 μm spectral signature is due to amphibole phases like tremolite or actinolite. As we have shown with the Lost City rock samples, the ''talc-rich fault rock'' and ''amphibole-rich fault rock'' look nearly identical in NIR measurements. Amphiboles have been detected in martian meteorites (*e.g.,* Williams *et al.,* 2014) and are possibly present on the surface of Mars. They are potentially present as spectral mixtures of saponite and hornblende (Carter *et al.,* 2013) but otherwise have not been discussed extensively in the martian literature. In the case of Nili Fossae, Viviano *et al.* (2013) noted the spectral ambiguity between talc and actinolite but argued that the presence of amphibole within the context of the mineral assemblage observed in the region is unlikely. While we agree that talc and/or talc + saponite are likely to be at least partially responsible for the ambiguous spectral signature in Nili Fossae given the nearby presence of magnesite, it is important to note that amphibole does fit into the common assemblage of minerals formed during serpentinization, as shown by the Lost City rock samples.

4.3. Spectral differences between measurements from the Lost City Hydrothermal Field and Nili Fossae, Mars

There are some clear differences between the spectral characteristics and mineralogy of the Lost City rock samples and the surface exposures in Nili Fossae, Mars. First, the Nili Fossae assemblage has abundant olivine still present within the stratigraphic section. The fact that abundant olivine remains, unaltered to serpentine (or magnesite), indicates that the serpentinization reactions in the area never went to completion, perhaps indicating limited alteration and/or water volume. Comparatively, the Lost City serpentinites and associated rocks used for this study show few signs of their unaltered protolith. The most mafic of the samples acquired is still an extensively altered metagabbro. However, cores drilled from the southern wall of the Atlantis Massif during the 2016 IODP Expedition 357 show evidence for variable serpentinization with depth (Früh-Green *et al.,* 2016).

Another mineralogical difference between the Lost City rocks used in this study and Nili Fossae surface exposures is the presence of different major-metal cations in their respective carbonates. The Lost City carbonates are dominated by either Ca-rich calcite or aragonite. Rocks formed via the accumulation of pelagic material (''pelagic top-layer rocks'') are dominated by calcite. However, the young hydrothermal chimneys are dominated by aragonite derived from mixing of high-pH hydrothermal fluids and seawater (''carbonates''). Because aragonite is metastable, aragonite in the chimneys reverts to calcite over time (Ludwig *et al.,* 2006). The Nili Fossae carbonate-bearing exposures are Mg-rich and spectrally consistent with magnesite.

There are several potential scenarios for the formation of the martian carbonate in Nili Fossae; one is via the direct alteration of the Mg-rich olivine in the area by near-surface water (Ehlmann *et al.,* 2008), which could also lead to the formation of talc as in the talc carbonation of komatiite layers preserved in the Archean greenstone sequences on Earth (Brown *et al.,* 2010). Another potential formation mechanism is the carbonation of the serpentine-bearing rocks (Viviano *et al.,* 2013). This process would not only produce the Mg-rich magnesite but also produce talc, which is also observed near the Mg carbonates in the region. The formation of carbonates detected in Nili Fossae and directly

observed and sampled in Lost City was likely produced by different processes. Formation of Lost City carbonates was through mixing of high pH hydrothermal fluids exiting the seafloor with seawater. In contrast, the carbonates produced in Nili Fossae, Mars, were likely produced during subsurface hydrothermal alteration of the bedrock by meteoric waters. This is one clear example of where the environmental analogue between the Lost City and Nili Fossae is not as strong, given the evidence currently at hand.

4.4. Implications for serpentinization in Nili Fossae, Mars

4.4.1. Physical characteristics of Nili Fossae and its susceptibility to serpentinization. The Nili Fossae region is one of several extensive exposures of olivine-rich basalt on Mars (*e.g.,* layers in Valles Marineris, Terra Tyrrhena, the rim of Argyre Basin) and has the highest olivine concentration, ~40 vol % (Ody *et al.,* 2013). Of the other olivine-enriched regions, it is the only one that shows spectral evidence for serpentine in association with other mineral phases known to form in a serpentinizing system. There are several factors that may have contributed to serpentinization in this area beyond just the necessary olivine-rich protolith. For example, the formation of the Nili Fossae likely occurred in association with the Isidis Basin impact event, creating a highly fractured terrain. In addition to the large, regional-scale fractures that make up the main Nili Fossae troughs, the basement phyllosilicate-bearing unit shows abundant local-scale ridges and fractures. They are typically hundreds of meters long and tens of meters wide and appear to be the source of the Fe/Mg-phyllosilicate spectral signatures (Mangold *et al.,* 2007; Mustard 2007, 2009; Ehlmann *et al.,* 2009, 2010).

Saper and Mustard (2013) showed that the orientation of most of the small-scale ridges and fractures lines up with the larger orientation of the main Nili Fossae troughs, implying that these ridges were emplaced by the same mechanism as the large-scale graben, around the same time. These local-scale faults, fractures, and dikes, in addition to the regional-scale fossae, would have allowed for substantial fluid circulation pathways. Additionally, there has likely been a long-lived heat-source in the region, induced by both the Isidis Basin impact event and formation of the Syrtis Major volcanic province. This early fractured bedrock, combined with the olivine-rich protolith, would have created an environment suitable for the initiation of serpentinization. Therefore, this region was likely susceptible to serpentinization reactions due to (1) the olivine-enriched protolith, (2) the Isidis impact event, which created fractured terrain and provided a heat source, and (3) proximity to the Syrtis Major volcano, which may have also provided an additional regional heat source. It is important to note, however, that the extensive remnants of olivine in the region imply that the serpentinization reactions did not go to completion and that water was likely a limiting resource in driving these reactions forward.

4.4.2. Mineralogical evidence for serpentinization. The spectra acquired from Nili Fossae are similar to those measurements acquired from rocks collected at the Lost City Hydrothermal Field. As noted by McSween *et al.* (2015), rather than looking for a single mineral that might be a ''smoking gun'' for a particular geochemical environment, the search for specific mineralogical *assemblages* can provide greater constraints on the environment in question and narrow the search for once-habitable environments. Furthermore, the observation of a suite of minerals indicative of a formation environment provides greater confidence that the environment was indeed present. Reliance on the detection of a singular spectral signature indicative of just one mineral phase is not as robust a result since the interpretation can be more easily confounded by spectral ambiguities and data artifacts.

At both the Lost City Hydrothermal Field and Nili Fossae, analyses conducted in this study documented Mg-serpentine phases; carbonate phases; and talc, saponite, and/or amphibole. Additionally, in Nili Fossae abundant olivine has been documented as well as a geological setting (described in Section 4.4.1) that would favor the transport and circulation of hydrothermal fluids. With the exception of serpentine, the other phases documented in Nili Fossae *could* form under non-serpentinizing conditions. For example, the Mg carbonate could be the direct product of near-surface aqueous alteration of the olivine-rich basalt. Similarly, saponite can form via the hydrothermal alteration of olivine-poor basalt. However, the presence of all these phases within the same stratigraphic unit, and within the same CRISM image, likely implies a connected geochemical story consistent with hydrothermal alteration of an olivine-rich protolith in the eastern portions of the Nili Fossae. Fluid circulation resulted in serpentinization at the subsurface interface between the olivine-rich basalt and underlying olivine-poor, phyllosilicate-bearing basalt. The serpentinite bedrock was subsequently altered by carbonation to talc and magnesite, consistent with their co-spatial occurrence across the eastern region of the Nili Fossae.

Though there is only one case of serpentine, Mg carbonate, and talc/saponite in the same CRISM scene (FRS0002AE17_01), given the wide distribution of all three phases across the Nili Fossae region (Fig. 8) within exposures of the olivine-rich basalt unit, these phases are likely related to each other. The limited number of CRISM scenes where all three phases are concurrent may be an observational bias due to limited exposures beneath the cap unit. The paucity of serpentine detections in general is consistent within the context of the observed mineral suite and the hypothesis of serpentine carbonation to form talc and magnesite. Lastly, as described in the previous paragraph, magnesite and saponite (which cannot be distinguished from talc from these observations) can form independently of serpentine; therefore, it may be that across the Nili Fossae region these phases originated from slightly different processes, all involving the alteration of olivine. Only locally, where the spectral evidence for serpentine is observed, can one confidently invoke serpentinization processes.

An important consideration is the timing of the serpentinization reactions. The alteration must have occurred subsequent to the emplacement of the olivine-rich basalt unit at approximately 4 Ga (Wichman and Schultz, 1989). According to the model put forward by Viviano *et al.* (2013), the suite of alteration minerals described here likely formed prior to the emplacement of the Hesperian-aged Syrtis lava flows, at approximately 3.7 Ga. The altered olivine-rich unit has subsequently been eroded by episodic aqueous processes, evidenced by channel networks that cut

through the Hesperian-aged lava flows, and atmospherically driven processes (*e.g.,* dunes and dust abrasion) that resulted in exposure of the suite of alteration minerals as seen today.

4.4.3. Implications for habitability of Nili Fossae, Mars. We have shown that the spectral signatures and mineralogical suites present at the Lost City Hydrothermal Field on Earth are similar to those documented in the Nili Fossae region of Mars. This suite of minerals is unique to serpentinization where the reduction of H_2O in the presence of Fe^{2+} generates H_2. Molecular hydrogen is particularly interesting from an astrobiological standpoint because it is a strong electron donor that can drive the synthesis of organic molecules in Fischer-Tropsch-type reactions (*e.g.,* Holm and Charlou, 2001; McCollom and Seewald, 2007; Proskurowski, *et al.,* 2008). Organic compounds such as various hydrocarbons, formate, and acetate are present at elevated concentrations in Lost City fluids (Proskurowski *et al.,* 2008; Lang *et al.,* 2010). The abiotic production of organic compounds is significant because they can be used as precursors to important biological polymers, and hydrothermal chimneys such as those at Lost City can act as efficient incubators and reaction vessels (Stüeken *et al.,* 2013; Kreysing *et al.,* 2015).

Furthermore, H_2 is directly used as an electron donor in the metabolism of many chemoautotrophic organisms (*e.g.,* Nealson *et al.,* 2005; Schulte *et al.,* 2006; Stüeken *et al.,* 2013). For example, methanogens, which are abundant in Lost City chimneys (Schrenk *et al.,* 2004; Brazelton *et al.,* 2011), use H_2 to fix CO_2 and produce CH_4 and H_2O. This pathway is thought to be one of the most ancient metabolic strategies (Fuchs, 2011), and the catalytic cores of enzymes in this pathway resemble minerals found in hydrothermal systems (Russell and Martin, 2004). These minerals can catalyze some steps of carbon fixation on their own without the scaffolding provided by enzymes, suggesting potential links to prebiotic chemistry (Cody, 2004; Stüeken *et al.,* 2013).

Many of the key pieces necessary for life are produced in rock-hosted serpentinizing systems: liquid water, an energy source, reducing power, and abiotically produced hydrocarbons. Given the evidence for serpentinization in Nili Fossae, it is possible that it could have had a habitable subsurface environment at some point in its history. Additionally, the fractured nature of the Nili Fossae terrain would have provided local-scale, high-permeability pathways that promoted fluid flow. Interaction of these fluids with the bedrock would likely have resulted in formation of H_2 and low-order organics, similar to fluids currently venting from chimneys at the Lost City Hydrothermal Field. The remnants of these fractures and faults would be compelling places to search for potential biosignatures from any hypothetical life in the past, or simply to better understand the range of abiotically produced organic compounds on Mars.

It should be acknowledged that it is known that serpentine can form without the production of H_2 (Reactions 2 and 3); however, in a natural setting with non–end-member olivine compositions (*i.e.,* fayalite versus forsterite), it is unlikely that only Reactions 2 and 3 would occur without Reaction 1. In particular, given the known olivine composition in Nili Fossae ($Fo_{68–75}$; Hoefen *et al.,* 2003; Hamilton and Christensen, 2005; Koeppen and Hamilton, 2008; Edwards and Ehlmann, 2015), we expect Reactions 1–3 to take place. To confirm the occurrence of H_2 production during serpentinization, future studies should search for the presence of magnetite or other Fe^{3+} phases (*e.g.,* Fe^{3+}-bearing brucite) in association with the serpentine, as these cannot be detected from current orbital data sets.

For many geological, chemical, physical, and biological reasons, serpentinite-hosted hydrothermal vent systems have been discussed as compelling environments for key steps in the origin of life on Earth before ~3.5 Ga (*e.g.,* Russell *et al.,* 2010, 2014; Stüeken *et al.,* 2013; Sojo *et al.,* 2016). The results of this study provide further evidence that similar geochemical systems would have been active on Mars during the same time period in our solar system's evolution.

5. Conclusions

The present study draws mineralogical and geochemical parallels between the Lost City Hydrothermal Field on Earth and the Nili Fossae region on Mars. There is abundant evidence that serpentinization occurred in the Nili Fossae region during an important time period on our own planet when life was first emerging. It is not possible to determine whether life inhabited serpentinizing systems on Mars from the remote sensing data alone. However, it is clear that habitable environments promoted by serpentinization processes may have been present.

There are several major geological and geochemical differences between the Lost City and Nili Fossae. For example, the initial fluid compositions were likely quite different. In addition, the Lost City Hydrothermal Field is located at a water depth of ~800 m and ~15 km away from a slow-spreading oceanic ridge. In contrast, serpentinization occurring at Nili Fossae would likely have taken place in the subsurface with a limited or variable water source. Regardless, the fact that serpentinization reactions require such readily available starting materials, and produce biologically accessible by-products, is what makes them so compelling for astrobiological study.

The presence of serpentine in Nili Fossae indicates that fluid-rock reactions took place, likely implying that H_2 and abiotically produced organic compounds were produced in the subsurface. As such, Nili Fossae, specifically where the local grouping of the mineralogical suite presented here was documented, is a compelling site to search for evidence of past life on Mars. Equally compelling is the opportunity to study a martian site that formed during the same time when similar geochemical sites on Earth likely led to the origin of life. Insights as to whether life inhabited these sites on Mars will have important implications for our understanding of how and why life evolved on our own planet.

Acknowledgments

We would like to thank the Mars Reconnaissance Orbiter operations teams for targeting, collecting, and archiving the CRISM data set used for this study. JMARS, Davinci, ISIS3, and GDAL software were used for data processing and analysis. Thermal-infrared measurements were made in the Thermal Emission Spectroscopy Laboratory at Arizona State University. The Lost City samples and subsequent work were supported by a NSF grant to D. Kelley (OCEO137206) at the University of Washington and to G. Früh-Green at ETH-Zurich (0-20890-1), and Swiss grants 2100068055 and 20020-107620. We would also like to thank Norman Sleep

and two anonymous reviewers for providing helpful and thorough reviews that significantly improved and clarified this manuscript. Funding for this project was provided in part by the Mars Data Analysis Program grant NNX14AM33G.

Author Disclosure

All authors state that no competing financial interests exist.

References

Abrajano, T.A., Sturchio, N.C., Bohlke, J.K., Lyon, G.L., Poreda, R.J., and Stevens, C.M. (1988) Methane-hydrogen gas seeps, Zambales ophiolite, Phillipines: deep or shallow origin? *Chem Geol* 71:211–222.

Amador, E.S. and Bandfield, J.L. (2016) Elevated bulk-silica exposures and evidence for multiple aqueous alteration episodes in Nili Fossae, Mars. *Icarus* 276:39–51.

Bandfield, J.L., Christensen, P.R., and Smith, M.D. (2000) Spectral data set factor analysis and end-member recovery: application to analysis of martian atmospheric particulates. *J Geophys Res* 105, doi:10.1029/1999JE001094.

Barnes, I., Neil, J., and Trescase, J.J. (1978) Present day serpentinization in New Caledonia, Oman and Yugoslavia. *Geochim Cosmochim Acta* 42:144–145.

Bibring J.-P, Soufflot, A., Berthé, M., Langevin, Y., Gondet, B., Drossart, P., Bouyé, M., Combes, M., Puget, P., Semery, A., Bellucci, G., Formisano, V., Moroz, V., Kottsov, V., Bonello, G., Erard, S., Forni, O., Gendrin, A., Manaud, N., Poulet, F., Poulleau, G., Encrenaz, T., Fouchet, T., Melchiori, R., Altieri, F., Ignatiev, N., Titov, D., Zasova, L., Coradini, A., Capacionni, F., Cerroni, P., Fonti, S., Mangold, N., Pinet, P., Schmitt, B., Sotin, C., Hauber, E., Hoffmann, H., Jaumann, R., Keller, U., Arvidson, R., Mustard, J., and Forget, F. (2004) OMEGA: Observatoire pour la Minéralogie, l'Eau, les Glaces et l'Activité. In *Mars Express: The Scientific Payload,* edited by A. Wilson, ESA Publication Division, ESTEC, Noordwijk, the Netherlands, pp 37–49.

Bibring, J.-P., Langevin, Y., Mustard, J.F., and Arvidson, R. (2006) Global mineralogical and aqueous Mars history derived from OMEGA/Mars Express data. *Science* 312:400–404.

Bishop, J.L., Lane, M.D., Dyar, M.D., and Brown, A.J. (2008) Reflectance and emission spectroscopy of four groups of phyllosilicates: smectites, kaolinite-serpentines, chlorites and micas. *Clay Miner* 43:35–54.

Boschi, C., Fruh-Green, G.L., Delacour, A., Karson, J.A., and Kelley, D.S. (2006) Mass transfer and fluid flow during detachment faulting and development of an oceanic core complex, Atlantis Massif (MAR 30°N). *Geochem Geophys Geosyst* 7, doi:10.1029/2005GC001074.

Brazelton, W.J., Schrenk, M.O., Kelley, D.S., and Baross, J. (2006) Methane- and sulfur-metabolizing microbial communities dominate the Lost City Hydrothermal Field ecosystem. *Appl Environ Microbiol* 72:6257–6270.

Brazelton, W.J., Ludwig, K.A., Sogin, M.L., Andreishcheva, E.N., Kelley, D.S., Shen, C., Edwards, R.L., and Baross, J.A. (2010) Archaea and bacteria with surprising microdiversity show shifts in dominance over 1,000-year time scales in hydrothermal chimneys. *Proc Natl Acad Sci USA* 107:1612–1617.

Brazelton, W.J., Mehta, M.P., Kelley, D.S., and Baross, J.A. (2011) Physiological differentiation within a single-species biofilm fueled by serpentinization. *mBio* 2, doi:10.1128/mBio.00127-11.

Brown, A.J., Cudahy, T.J., and Walter, M.R. (2004) Short wave infrared reflectance investigation of sites of palaeobiological interest: applications for Mars exploration. *Astrobiology* 4:359–376.

Brown, A.J., Walter, M.R., and Cudahy, T.J. (2005) Hyperspectral imaging spectroscopy of a Mars analog environment at the North Pole Dome, Pilbara Craton, Western Australia. *Australian Journal of Earth Sciences* 52:353–364.

Brown, A.J., Hook, S.J., Baldridge, A.M., Crowley, J.K., Bridges, N.T., Thomson, B.J., Marion, G.M., de Souza Filho, C.R., and Bishop, J.L. (2010) Hydrothermal formation of clay-carbonate alteration assemblages in the Nili Fossae region of Mars. *Earth Planet Sci Lett* 297:174–182.

Carr, M.H. and Head, J.W. (2016) Geologic history of Mars. *Earth Planet Sci Lett* 294:185–203.

Carter, J., Poulet, F., Bibring, J.-P., Mangold, N., and Murchie, S. (2013) Hydrous minerals on Mars as seen by the CRISM and OMEGA imaging spectrometers: updated global view. *J Geophys Res: Planets* 118:831–858.

Charlou, J.L., Donval, J.P., Fouquet, Y., Jean-Baptiste, P., and Holm, N. (2002) Geochemistry of high H_2 and CH_4 vent fluids issuing from ultramatic rocks at the Rainbow hydrothermal field (36°14′N, MAR). *Chem Geol* 191:345–359.

Christensen, P.R., Bandfield, J.L., Hamilton, V.E., Howard, D.A., Lane, M.D., Piatek, J.L., Ruff, S.W., and Stefanov, W.L. (2000) A thermal emission spectral library of rock-forming minerals. *J Geophys Res* 105:9735–9739.

Clark, R.N., Swayze, G.A., Wise, R., Livo, E., Hoefen, T., Kokaly, R., and Sutley, S.J. (2007) *USGS Digital Spectral Library splib06a,* Digital Data Series 231, U.S. Geological Survey, Reston, VA.

Cody, G.D. (2004) Transition metal sulfides and the origins of metabolism. *Annu Rev Earth Planet Sci* 32:569–599.

Cuadros, J., Dekov, V.M., and Diore, S. (2008) Crystal chemistry of the mixed-layer sequence talc-talc-smectite-smectite from submarine hydrothermal vents. *Am Mineral* 93:1338–1348.

Delacour, A., Früh-Green, G.L., Bernasconi, S.M., Schaeffer, P., and Kelley, D.S. (2008) Carbon geochemistry of serpentinites in the Lost City Hydrothermal System (30°N, MAR). *Geochim Cosmochim Acta* 72:3681–3702.

Denny, A.R., Kelley, D.S., and Fruh-Green, G.L. (2016) Geologic evolution of the Lost City Hydrothermal Field. *Geochem Geophys Geosyst* 17:375–394.

Domagal-Goldman, S.D., Wright, K.E., Adamala, K., Anderson, R., Arney, G., Atri, D., Azua-Bustos, A., Bowman, J.S., Brazelton, W.J., Brennecka, G.A., Carns, R., Chopra, A., Colangelo-Lillis, J., Crockett, C.J., DeMarines, J., Frank, E.A., Frantz, C., de la Fuente, E., Galante, D., Glass, J., Gleeson, D., Glein, C.R., Goldblatt, C., Horak, R., Horodyskyj, L., Kacar, B., Kereszturi, A., Knowles, E., Mayeur, P., Mcglynn, S., Miguel, Y., Montgomery, M., Neish, C., Noack, L., Rugheimer, S., Stueken, E.E., Tamez-Hidalgo, P., Walker, S.I., and Wong, T. (2016) The Astrobiology Primer v2.0. *Astrobiology* 16:561–653.

Edwards, C.S. and Ehlmann, B.L. (2015) Carbon sequestration on Mars. *Geology* 43, doi:10.1130/G36983.1.

Ehlmann, B.L., Mustard, J.F., Murchie, S.L., Poulet, F., Bishop, J.L., Roach, L.H., Roush, T.L., Swayze, G.A., and Wray, J.J. (2008) Orbital identification of carbonate-bearing rocks on Mars. *Science* 322:1828–1832.

Ehlmann, B.L., Mustard, J.F., Swayze, G.A., Clark, R.N., Bishop, J.L., Poulet, F., Des Marais, D.J., Roach, L.H., Milliken, R.E., Wray, J.J., Barnouin-Jha, O., and Murchie,

S.L. (2009) Identification of hydrated silicate minerals on Mars using MRO-CRISM: geologic context near Nili Fossae and implications for aqueous alteration. *J Geophys Res: Planets* 114, doi:10.1029/2009JE003339.

Ehlmann, B.L., Mustard, J.F., and Murchie, S.L. (2010) Geologic setting of serpentine deposits on Mars. *Geophys Res Lett* 37, doi:10.1029/2010GL042596.

Etiope, G., Schoell, M., and Hosgrmez, H. (2011) Abiotic methane flux from the Chimaera seep and Tekirova ophiolites (Turkey): understanding gas exhalation from low temperature serpentinization and implications for Mars. *Earth Planet Sci Lett* 310:96–104.

Evans, B.W. (1977) Metamorphism of alpine peridotite and serpentinite. *Annu Rev Earth Planet Sci* 5:397–447.

Evans, B.W. (2004) The serpentinite multisystem revisited: chrysotile is metastable. *Int Geol Rev* 46:479–506.

Evans, B.W. (2010) Lizardite versus antigorite serpentinite: magnetite, hydrogen, and life (?). *Geology* 38:879–882.

Evans, B.W. and Guggenheim, S. (1988) Talc, pyrophyllite, and related minerals. In *Hydrous Phyllosilicates (Exclusive of Micas),* edited by S.W. Bailey, Reviews in Mineralogy Volume 19, Mineralogical Society of America, Washington, DC, pp 225–294.

Feely, K.C. and Christensen, P.R. (1999) Quantitative compositional analysis using thermal emission spectroscopy: application to igneous and metamorphic rocks. *J Geophys Res: Planets* 104:24195–24210.

Frey, H.V. (2003) Buried impact basins and the earliest history of Mars [abstract 3104]. In *35th Lunar and Planetary Science Conference,* Lunar and Planetary Institute, Houston.

Früh-Green, G.L., Kelley, D.S., Bernasconi, S.M., Karson, J.A., Ludwig, K.A., Butterfield, D.A., Boschi, C., and Proskurowski, G. (2003) 30,000 years of hydrothermal activity at the Lost City Hydrothermal Field. *Science* 301: 495–498.

Früh-Green, G.L., Connolly, J.A.D., Plas, A., Kelley, D.S., and Groberty, B. (2004) Serpentinization of oceanic peridotites: implications for geochemical cycles and biological activity. In *The Subseafloor Biosphere at Mid-Ocean Ridges,* edited by W.S.D. Wilcock, E.F. DeLong, D.S. Kelley, J.A. Baross, and S.C. Cary, Geophysical Monograph Series 144, American Geophysical Union, Washington, DC, pp 119–136.

Früh-Green, G.L., Orcutt, B.N., Green, S., Cotterill, C., and the Expedition 357 Scientists. (2016) *Expedition 357 Preliminary Report: Atlantis Massif Serpentinization and Life,* International Ocean Discovery Program. Available online at http://dx.doi.org/10.14379/iodp.pr.357.2016

Fuchs, G. (2011) Alternative pathways of carbon dioxide: insights into the early evolution of life? *Annu Rev Microbiol* 65:631–658.

Gaffey, S. (1987) Theory. Mn^{2+} and Fe^{2+} produce very strong using the Gaussian fitting (GFIT) routine. *J Geophys Res* 92: 1429–1440.

Hamilton, V.E. and Christensen, P.R. (2000) Determining the modal mineralogy of mafic and ultramafic igneous rocks using thermal emission spectroscopy. *J Geophys Res: Planets* 105:9717–9733.

Hamilton, V.E. and Christensen, P.R. (2005) Evidence for extensive olivine-rich bedrock in Nili Fossae, Mars. *Geology* 33:433–436.

Hodgkinson, M.R.S., Webber, A.P., Roberts, S., Mills, R.A., Connelly, D.P., and Murton, B.J. (2015) Talc-dominated seafloor deposits reveal a new class of hydrothermal system. *Nat Commun* 6, doi:10.1038/ncomms10150.

Hoefen, T.M., Clark, R.N., Bandfield, J.L., Smith, M.D., Pearl, J.C., and Christensen, P.R. (2003) Discovery of olivine in the Nili Fssae region of Mars. *Science* 302:627–630.

Holm, N.G. and Charlou, J.L. (2001) Initial indications of abiotic formation of hydrocarbons in the Rainbow ultramafic hydrothermal system, Mid-Atlantic Ridge. *Earth Planet Sci Lett* 191, doi:10.1016/S0012-821X(01)00397-1.

Hunt, G.R. (1980) Electromagnetic radiation: the communication link in remote sensing. In *Remote SENSING in Geology,* edited by B.S. Siegel and A.R. Gillespie, John Wiley, New York, pp 5–45.

Hunt, G.R. and Salisbury, J.W. (1971) Visible and near-infrared spectra of minerals and rocks: II carbonates. *Modern Geology* 2:23–30.

Karson, J.A., Früh-Green, G.L., Kelley, D.S., Williams, E.A., Yoerger, D.R., and Jakuba, M. (2006) Detachment shear zone of the Atlantis Massif core complex, Mid-Atlantic Ridge, 30°N. *Geochem Geophys Geosyst* 7, doi:10.1029/2005GC001109.

Kelley, D.S. and Früh-Green, G.L. (1999) Abiogenic methane in deep-seated mid-ocean ridge environments: insights from stable isotope analyses. *J Geophys Res* 104:10439–10460.

Kelley, D.S., Karson, J.A., Butter, D.A., Lilley, M.D., Blackman, D.K., Früh-Green, G.L., Olson, E.J., Schrenk, M.O., Roe, K.K., Lebon, G.T., Rivizzigno, P., and the AT3-60 Ship Party. (2001) An off-axis hydrothermal vent field near the Mid-Atlantic Ridge at 30°N. *Nature* 412:145–149.

Kelley, D.S., Karson, J.A., Früh-Green, G.L., Yoerger, D.R., Shank, T.M., Butterfield, D.A., Hayes, J.M., Schrenk, M.O., Olson, E.J., Proskurowski, G., Jakuba, M., Bradley, A., Larson, B., Ludwig, K., Glickson, D., Buckman, K., Bradley, A.S., Brazelton, W.J., Roe, K., Elend, M.J., Delacour, A., Bernasconi, S.M., Lilley, M.D., Baross, J.A., Summons, R.E., and Sylva, S.P. (2005) A serpentinite-hosted ecosystem: the Lost City Hydrothermal Field. *Science* 307:1428–1434.

King, T.V.V. and Clark, R.N. (1989) Spectral characteristics of chlorites and Mg-serpentines using high-resolution reflectance spectroscopy. *J Geophys Res* 94(B10):13997–14008.

Klein, F. and McCollom, T.M. (2013) From serpentinization to carbonation: new insights from a CO_2 injection experiment. *Earth Planet Sci Lett* 379:137–145.

Koeppen, W.C. and Hamilton, V.E. (2008) Global distribution, composition, and abundance of olivine on the surface of Mars from thermal infrared data. *J Geophys Res* 113, doi:10.1029/2007JE002984.

Kreysing, M., Keil, L., Lanzmich, S., and Braun, D. (2015) Heat flux across an open pore enables the continuous replication and selection of oligonucleotides towards increasing length. *Nat Chem* 7:203–208.

Lane, M.D. (1999) Midinfrared optical constants of calcite and their relationship to particle size effects in thermal emission spectra of granular calcite. *J Geophys Res: Planets* 104: 14099–14108.

Lang, S.Q., Butterfield, D.A., Schulte, M., Kelley, D.S., and Lilley, M.D. (2010) Elevated concentrations of formate, acetate and dissolved organic carbon found at the Lost City Hydrothermal Field. *Geochim Cosmochim Acta* 74:941–952.

López-Garcia, P., Vereshchaka, A., and Moreira, D. (2007) Eukaryotic diversity associated with carbonates and fluid-seawater interface in Lost City Hydrothermal Field. *Environ Microbiol* 9:546–554.

Lowell, R.P. and Rona, P.A. (2002) Seafloor hydrothermal systems driven by the serpentinization of peridotite. *Geophys Res Lett* 29, doi:10.1029/2001GL014411.

Ludwig, K.A., Kelley, D.S., Butterfield, D.A., Nelson, B.K., and Früh-Green, G.F. (2006) Formation and evolution of carbonate chimneys at the Lost City Hydrothermal Field. *Geochim Cosmochim Acta* 70:3625–3645.

Ludwig, K.A., Shen, C.-C., Kelley, D.S., Cheng, H., and Edwards, R.L. (2011) U–Th systematics and ^{230}Th ages of carbonate chimneys at the Lost City Hydrothermal Field. *Geochim Cosmochim Acta* 75:1869–1888.

Lyon, R.J.P. (1965) Analysis of rocks by spectral infrared emission (8 to 25 microns). *Econ Geol* 60:715–736.

Malamud, U. and Prialnik, D. (2013) Modeling serpentinization: applied to the early evolution of Enceladus and Mimas. *Icarus* 225:763–774.

Malinowski, E.R. (1991) *Factor Analysis in Chemistry,* 2nd ed., John Wiley, New York.

Mangold, N., Poulet, F., Mustard, J.F., Bibring, J.-P., Gondet, V., Langevin, Y., Ansan, V., Masson, Ph., Fassett, C., Head III, J.W., Hoffmann, H., and Neukum, G. (2007) Mineralogy of the Nili Fossae region with OMEGA/Mars Express data: 2. Aqueous alteration of the crust. *J Geophys Res: Planets* 112: E08S04, doi:10.1029/2006JE002835.

Martin, W., Baross, J., Kelley, D., and Russell, M.J. (2008) Hydrothermal vents and the origin of life. *Nat Rev Microbiol* 6:805–814.

McCollom, T.M. and Seewald, J.S. (2007) Abiotic synthesis of organic compounds in deep-sea hydrothermal environments on abiotic synthesis. *Chem Rev* 107:382–401.

McGuire, P.C., Bishop, J.L., Brown, A.J., Fraeman, A.A., Marzo, G.A., Frank Morgan, M., Murchie, S.L., Mustard, J.F., Parente, M., Pelkey, S.M., Roush, T.L., Seelos, F.P., Smith, M.D., Wendt, L., and Wolff, M.J. (2009) An improvement to the volcano-scan algorithm for atmospheric correction of CRISM and OMEGA spectral data. *Planet Space Sci* 57:809–815.

McSween, H.Y., Labotka, T.C., and Viviano-Beck, C.E. (2015) Metamorphism in the martian crust. *Meteorit Planet Sci* 50:590–603.

Michalski, J.R., Cuadros, J., Bishop, J.L., Darby Dyar, M., Dekov, V., and Fiore, S. (2015) Constraints on the crystal-chemistry of Fe/Mg-rich smectitic clays on Mars and links to global alteration trends. *Earth Planet Sci Lett* 427:215–225.

Moore, D.E. and Rymer, M.J. (2007) Talc-bearing serpentinite and the creeping section of the San Andreas fault. *Nature* 448:795–797.

Murchie, S., Arvidson, R.E., Bedini, P., Beisser, K., Bibring, J.-P., Bishop, J., Boldt, J., Cavender, P., Choo, T., Clancy, R.T., Darlington, E.H., Des Marais, D., Espiritu, R., Fort, D., Green, R., Guinness, E., Hayes, J., Hash, C., Heffernan, K., Hemmler, J., Heyler, G., Humm, D., Hutcheson, J., Izenberg, N., Lee, R., Lees, J., Lohr, D., Malaret, E., Martin, T., McGovern, J.A., McGuire, P., Morris, R., Mustard, J., Pelkey, S., Rhodes, E., Robinson, M., Roush, T., Schaefer, E., Seagrave, G., Seelos, F., Silverglate, P., Slavney, S., Smith, M., Shyong, W.J., Strohbehn, K., Taylor, H., Thompson, P., Tossman, B., Wirzburger, M., and Wolff, M. (2007) Compact Reconnaissance Imaging Spectrometer for Mars (CRISM) on Mars Reconnaissance Orbiter (MRO). *J Geophys Res: Planets* 112, doi:10.1029/2006JE002682.

Mustard, J.F., Poulet, F., Head, J.W., Mangold, N., Bibring, J.-P., Pelkey, S.M., Fassett, C.I., Langevin, Y., and Neukum, G. (2007) Mineralogy of the Nili Fossae region with OMEGA/Mars Express data: 1. Ancient impact melt in the Isidis Basin and implications for the transition from the Noachian to Hesperian. *J Geophys Res* 112, doi:10.1029/2006JE002834.

Mustard, J.F., Ehlmann, B.L., Murchie, S.L., Poulet, F., Mangold, N., Head, J.W., Bibring, J.P., and Roach, L.H. (2009) Composition, morphology, and stratigraphy of Noachian crust around the Isidis Basin. *J Geophys Res: Planets* 114, doi:10.1029/2009JE003349.

Neal, S. and Stanger, G. (1983) Hydrogen generation from mantle source rocks in Oman. *Earth Planet Sci Lett* 66:315–320.

Nealson, K.H., Inagaki, F., and Takai, K. (2005) Hydrogen-driven subsurface lithoautotrophic microbial ecosystems (SLiMEs): do they exist and why should we care? *Trends Microbiol* 13, doi: 10.1016/j.tim.2005.07.010.

Neubeck, A., Duc, N.T, Hellevang, H., Oze, C., Bastviken, D., Bacsik, Z., and Holm, N.G. (2014) Olivine alteration and H_2 production in carbonate-rich, low temperature aqueous environments. *Planet Space Sci* 96:51–61.

Ody, A., Poulet, F., Bibring, J.-P., Loizeau, D., Carter, J., Gondet, B., and Langevin, Y. (2013) Global investigation of olivine on Mars: insights into crust and mantle compositions. *J Geophys Res: Planets* 118:234–262.

O'Hanley, D.S. (1996) *Serpentinites: Records of Tectonics and Petrological History,* Oxford University Press, New York.

Palandri, J.L. and Reed, M.H. (2004) Geochemical models of metasomatism in ultramafic systems: serpentinization, rodingitization, and sea floor carbonate chimney precipitation. *Geochim Comochim Acta* 68:1115–1133.

Pelkey, S.M., Mustard, J.F., Murchie, S., Clancy, R.T., Wolff, M., Smith, M., Milliken, R.E., Bibring, J.P., Gendrin, A., Poulet, F., Langevin, Y., and Gondet, B. (2007) CRISM multispectral summary products: parameterizing mineral diversity on Mars from reflectance. *J Geophys Res: Planets* 112, doi:10.1029/2006JE002831.

Petersen, S., Kuhn, K., Kuhn, T., Augustin, N., Hékinian, R., Franz, L., and Borowski, C. (2009) The geological setting of the ultramafic-hosted Logatchev Hydrothermal Field (14°45′N, Mid-Atlantic Ridge) and its influence on massive sulfide formation. *Lithos* 112:40–56.

Poulet, F., Bibring, J.-P., Mustard, J.F., Gendrin, A., Mangold, N., Langevin, Y., Arvidson, R.E., Gondet, B., Gomez, C., Berthé, M., Erard, S., Forni, O., Manaud, N., Poulleau, G., Soufflot, A., Combes, M., Drossart, P., Encrenaz, T., Fouchet, T., Melchiorri, R., Bellucci, G., Altieri, F., Formisano, V., Fonti, S., Capaccioni, F., Cerroni, P., Coradini, A., Korablev, O., Kottsov, V., Ignatiev, N., Titov, D., Zasova, L., Pinet, P., Schmitt, B., Sotin, C., Hauber, E., Hoffmann, H., Jaumann, R., Keller, U., and Forget, F. (2005) Phyllosilicates on Mars and implications for early martian climate. *Nature* 438:623–627.

Proskurowski, G., Lilley, M.D., Kelley, D.S., and Olson, E.J. (2006) Low temperature volatile production at the Lost City Hydrothermal Field, evidence from a hydrogen stable isotope geothermometer. *Chem Geol* 229:331–343.

Proskurowski, G., Lilley, M.D., Seewald, J.S., Früh-Green, G.L., Olson, E.J., Lupton, J.E., Sylva, S.P., and Kelley, D.S. (2008) Abiogenic hydrocarbon production at Lost City Hydrothermal Field. *Science* 319:604–607.

Ramsey, M.S. and Christensen, P.R. (1998) Mineral abundance determination: quantitative deconvolution of thermal emission spectra. *J Geophys Res* 103, doi:10.1029/97JB02784.

Rogers, A.D. and Aharonson, O. (2008) Mineralogical composition of sands in Meridiani Planum determined from Mars Exploration rover data and comparison to orbital measurements. *J Geophys Res: Planets* 113, doi:10.1029/2007JE002995.

Ruff, S.W. and Christensen, P.R. (2002) Bright and dark regions on Mars: particle size and mineralogical characteristics

based on Thermal Emission Spectrometer data. *J Geophys Res* 107, doi:10.1029/2001JE001580.

Ruff, S.W., Christensen, P.R., Barbera, P.W., and Anderson, D.L. (1997) Quantitative thermal emission spectroscopy of minerals: a laboratory technique for measurement and calibration. *J Geophys Res: Solid Earth* 102:14899–14913.

Russell, M.J. and Martin, W. (2004) The rocky roots of the acetyl-CoA pathway. *Trends Biochem Sci* 29, doi:10.1016/j.tibs.2004.05.007.

Russell, M.J., Hall, A.J., and Martin, W. (2010) Serpentinization as a source of energy at the origin of life. *Geobiology* 8:355–371.

Russell, M.J., Barge, L.M., Bhartia, R., Bocanegra, D., Bracher, P.J., Branscomb, E., Kidd, R., Mcglynn, S., Meier, D.H., Nitschke, W., Shibuya, T., Vance, S., White, L., and Kanik, I. (2014) The drive to life on wet and icy worlds. *Astrobiology* 14:308–343.

Saper, L. and Mustard, J.F. (2013) Extensive linear ridge networks in Nili Fossae and Nilosyrtis, Mars: implications for fluid flow in the ancient crust. *Geophys Res Lett* 40:245–249.

Schrenk, M.O., Kelley, D.S., Bolton, S.A., and Baross, J.A. (2004) Low archaeal diversity linked to subseafloor geochemical processes at the Lost City Hydrothermal Field, Mid-Atlantic Ridge. *Environ Microbiol* 6:1086–1095.

Schulte, M., Blake, D., Hoehler, T., and McCollom, T. (2006) Serpentinization and its implications for life on the early Earth and Mars. *Astrobiology* 6:364–376.

Schultz, R.A. and Frey, H.V. (1990) A new survey of multiring impact basins on Mars. *J Geophys Res* 95:14175–14189.

Sojo, V., Herschy, B., Whicher, A., Camprubi, E., and Lane, N. (2016) The origin of life in alkaline hydrothermal vents. *Astrobiology* 16:181–197.

Stüeken, E.E., Anderson, R.E., Bowman, J.S., Brazelton, W.J., Colangelo-Lillis, J., Goldman, A.D., Som, S.M., and Baross, J.A. (2013) Did life originate from a global chemical reactor? *Geobiology* 11:101–126.

Thomas, N.H. and Bandfield, J.L. (2017) Identification and refinement of martian surface mineralogy using factor analysis and target transformation of near-infrared spectroscopic data. *Icarus* 291:124–135.

Thomas, N.H., Bandfield, J.L., and Amador, E.S. (2014) Identification and characterization of martian serpentine using target transformation and CRISM data [abstract 1909]. In *45th Lunar and Planetary Science Conference,* Lunar and Planetary Institute, Houston.

Thomson, J.L. and Salisbury, J.W. (1993) The mid-infrared reflectance of mineral mixtures (7–14 microns). *Remote Sens Environ* 45, doi:10.1016/0034-4257(93)90077-B.

Tornabene, L.L., Moersch, J.E., McSween, H.Y., Hamilton, V.E., Piatek, J.L., and Christensen, P.R. (2008) Surface and crater-exposed lithologic units of the Isidis based as mapped by coanalysis of THEMIS and TES derived data products. *J Geophys Res: Planets* 113, doi:10.1029/2007JE002988.

Vance, S., Harnmeijer, J., Kimura, J.U.N., Hussmann, H., Demartin, B., Brown, J.M., and Al, V.E.T. (2007) Hydrothermal systems in small ocean planets. *Astrobiology* 7:987–1005.

Viviano, C.E., Moersch, J.E., and McSween, H.Y. (2013) Implications for early hydrothermal environments on Mars through the spectral evidence for carbonation and chloritization reactions in the Nili Fossae region. *J Geophys Res: Planets* 118:1858–1872.

Viviano-Beck, C.E. and Murchie, S.L. (2014) Hydrothermally altered stratigraphy in the walls of Valles Marineris [abstract 1963]. In *45th Lunar and Planetary Science Conference,* Lunar and Planetary Institute, Houston.

Viviano-Beck, C.E., Seelos, F.P., Murchie, S.L., Kahn, E.G., Seelos, K.D., and Morgan, M.F. (2014) Revised CRISM spectral parameters and summary products based on the currently detected mineral diversity on Mars. *J Geophys Res: Planets* 119:1403–1431.

Wichman, R.W. and Schultz, P.H. (1989) Sequence and mechanisms of deformation around the Hellas and Isidis impact basins on Mars. *J Geophys Res* 94:17333–17357.

Wicks, F.J. and O'Hanley, D.S. (1988) Serpentines: Structures and petrology. In *Mineralogical Society of America Reviews in Mineralogy* 19:91–168.

Williams, K.B., Sonzogni, Y., and Treiman, A.H. (2014) Amphibole in the Tissant martian meteorite: composition and implication for volatile content of parental magma [abstract 1435]. In *45th Lunar and Planetary Science Conference,* Lunar and Planetary Science Institute, Houston.

Address correspondence to:
Elena S. Amador
Department of Earth and Space Sciences
University of Washington
Johnson Hall Rm-070, Box 351310
4000 15th Ave NE
Seattle WA, 98195-1310

E-mail: esamador@u.washington.edu

Submitted 17 October 2016
Accepted 14 April 2017

Abbreviations Used

CRISM = Compact Reconnaissance Imaging Spectrometer for Mars
FRS = full-resolution short
FRT = full-resolution targeted
HRL = half-resolution long
HRS = half-resolution short
NIR = near-infrared
TES = Thermal Emission Spectrometer
TIR = thermal-infrared